A multi-method approach to the study of hydrogen trapping in a maraging stainless steel: the impact of B2-NiAl precipitates and austenite

Jolan Bestautte, Abdelali Oudriss, Matthieu Lenci, Denis Bechet, Zacharie Obadia, Xavier Feaugas, Frédéric Christien

▶ **To cite this version:**

Jolan Bestautte, Abdelali Oudriss, Matthieu Lenci, Denis Bechet, Zacharie Obadia, et al.. A multi-method approach to the study of hydrogen trapping in a maraging stainless steel: the impact of B2-NiAl precipitates and austenite. Corrosion Science, 2023, 224, pp.111509. 10.1016/j.corsci.2023.111509 . emse-04370953

HAL Id: emse-04370953

https://hal-emse.ccsd.cnrs.fr/emse-04370953

Submitted on 20 Mar 2024

HAL is a multi-disciplinary open access archive for the deposit and dissemination of scientific research documents, whether they are published or not. The documents may come from teaching and research institutions in France or abroad, or from public or private research centers.

L'archive ouverte pluridisciplinaire **HAL**, est destinée au dépôt et à la diffusion de documents scientifiques de niveau recherche, publiés ou non, émanant des établissements d'enseignement et de recherche français ou étrangers, des laboratoires publics ou privés.

A multi-method approach to the study of hydrogen trapping in a maraging stainless steel: the impact of B2-NiAl precipitates and austenite

J. Bestautte[1], A. Oudriss[2], M. Lenci[1], D. Bechet[3], Z. Obadia[4], X. Feaugas[2], F. Christien[1]

[1] Mines Saint-Etienne, Univ Lyon, CNRS, UMR 5307 LGF, Centre SMS, F - 42023 Saint-Etienne, France

[2] La Rochelle University, LaSIE UMR CNRS 7356, La Rochelle, 17000, France

[3] Aubert & Duval, 63770 Les Ancizes, France

[4] Airbus Commercial, Toulouse, France

Abstract

The trapping behavior of hydrogen in a Fe-Cr-Ni-Al-Mo alloy (PH13-8Mo martensitic stainless steel) was investigated. Three different metallurgical states of the same alloy were obtained by heat treatment in an attempt to separate the impact of different microstructural features on the hydrogen trapping behavior. Microstructure analysis including dislocation density measurements and characterization of B2-NiAl precipitates and reverted austenite was conducted, using mainly X-ray Diffraction and Transmission Electron Microscopy. From electrochemical permeation conducted under varying hydrogen fugacity, the trapping characteristics (binding energy, trap density) of the three metallurgical states studied were first determined using the analytical one trap model of Kumnick and Johnson. Another more sophisticated numerical model was then developed in order to introduce two different types of traps. This model was used to simulate the permeation curves and the trapping characteristics were identified using an inverse approach. In a separate approach, Thermal Desorption Spectroscopy was also used to determine the trapping energies and the amount of hydrogen stored in different traps. Combination of these different experimental and modelling approaches have produced consistent results. It is shown that low-misfit coherent B2-NiAl precipitates have a very limited trapping capability. The high dislocation density, including dislocation walls (martensite lath boundaries), significantly traps hydrogen, at an intermediate energy of about 35 kJ/mol. Filmy reverted austenite has a double impact: hydrogen is trapped both at the martensite-austenite interfaces (~35 kJ/mol) and in the austenite bulk (20 kJ/mol).

Keywords

Maraging Steel; Hydrogen Diffusion and Trapping; Microstructure; Electrochemical Permeation; Thermal Desorption Spectroscopy; Modeling

1. Introduction

Precipitation-hardened martensitic steels, known as maraging steels, are widely used in numerous industrial fields where their high tensile strength and high fracture toughness are praised for the fabrication of critical components. The development of stainless maraging steels added the possibility to use these materials in corrosive environments. However, the exposition of both non-stainless and stainless maraging steels to hydrogen – which is a common product of corrosion reactions – has proven to be detrimental for their mechanical properties [1]. The origin of a material sensitivity to hydrogen embrittlement is believed to lie in both the hydrogen concentration and mobility [2,3]. A material ability to store a high concentration of hydrogen, as well as the mobility of hydrogen in the material bulk, are strongly dependant of the microstructure. For these reasons, the relations between microstructural features and hydrogen diffusion and trapping have been widely studied over the past decades. However, the complex microstructure of maraging steels makes it difficult to identify the individual contribution of microstructural components to the hydrogen trapping [4].

In a recent paper [5], *Bestautte et al.* studied hydrogen assisted quasi-cleavage in PH13-8Mo steel using tensile testing under in-situ cathodic charging, as well as post-mortem EBSD analysis of quasi-cleavage cracks. They showed that quasi-cleavage cracks propagate sub-critically in the microstructure. Quasi-cleavage consisted of very brittle cleavage cracks, connected by ductile ridges. The plastic activity was concentrated in the ductile ridges, i.e. between brittle cracks, not in the vicinity of them. The brittle part of cracks did not follow any type of interfaces. Instead, they propagated along {100} type crystal planes across individual martensite blocks. Sub-critical propagation involves hydrogen dynamic accumulation at the crack tip, which implies a sufficient mobility of hydrogen. Deep trapping of hydrogen in particular microstructural features can then be beneficial, as it will efficiently reduce its mobility.

Commonly the hydrogen state in the material is characterized by the interaction energy between the solute and the microstructure which define the trapping conditions [6]. The methods used to quantify hydrogen trapping give access to different type of energies which need to be clearly defined [7]. *Fig.* 1 (a) presents the different energies involved in the trapping process. The activation energy for hydrogen lattice diffusion is referred to as E_a, and the lattice sites are separated by a distance λ. The saddle point energy is the energy required for hydrogen to jump from a lattice site into a trap position and is noted E_S. The energy required to withdraw a hydrogen atom from a trap site is the trapping energy E_T. The difference of energy between a trap position and a lattice position is the binding energy E_B. Consequently, the following relation is obtained:

$$E_T = E_B + E_S \quad (1)$$

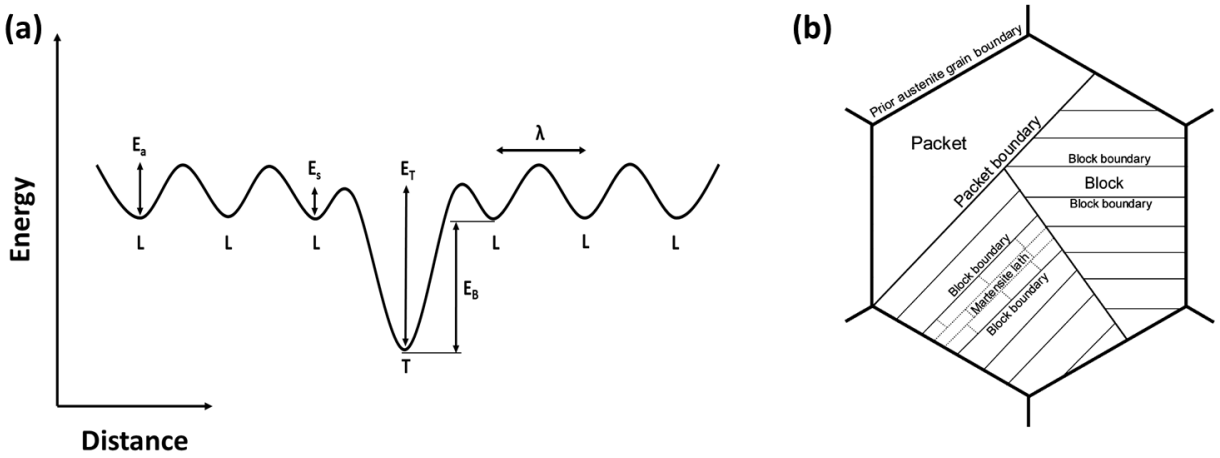

Fig. 1. Schematic representation of the different parameters used to describe hydrogen diffusion and trapping inside a crystalline structure (a) and schematic view of martensitic microstructure (b).

The multi-scale structure of martensite *Fig.* 1 (b), composed of former austenitic grains subdivided into packets, blocks and laths, presents a high density of interfaces. Hydrogen is known to interact with grain boundaries, and these interactions are governed by the nature of the grain boundaries [8–10]. *Oudriss et al.* [9] studied the specific effect of different types of boundaries in pure FCC nickel. They concluded that high-angle (random) boundaries act as short circuits for hydrogen diffusion. On the other hand, low misorientation grain boundaries and ordered boundaries act as trapping sites for hydrogen, because these boundaries can be accommodated by dislocations and vacancies, which actively trap hydrogen. They also found that when the ordered boundaries density becomes significant, the short-circuit diffusion along random boundaries has little impact on the global hydrogen diffusivity. In BCC materials, the impact of grain boundaries on the global diffusivity is lower than for FCC materials, in relation with higher lattice diffusivity [8]. In the case of a martensitic structure, the low misorientation boundaries are predominant (mainly because laths boundaries are low misorientation boundaries), so it is assumed that short-circuit diffusion along random boundaries has little influence on the diffusion of hydrogen inside the material. Moreover, the lath boundaries can be treated as dislocations walls [11,12], which is convenient to estimate their impact on hydrogen trapping in relation with a misorientation accommodated by geometrically necessary dislocation (GND) density.

It has been well established that dislocations play a major role for hydrogen trapping [13,14]. The martensitic structure shows a high dislocation density, making dislocations the primary traps for hydrogen in martensite [15]. First principle calculations confirmed that hydrogen can be trapped both in dislocation core and stress field, and for both screw and edge dislocations in BCC-Fe [16,17]. However, the trapping energy at dislocation core is higher than in dislocation elastic field [18].

The maraging steels are hardened through precipitation of one or multiple intermetallic phases. It is well established that the precipitation state and the nature of precipitates have a strong effect on hydrogen trapping [4,19–22]. *Peral et al.* [23] evidenced an increase in hydrogen trapping energy from 13 kJ/mol to 35 kJ/mol when adding vanadium to a Cr-Mo low alloy steel, which changed the precipitates nature from Cr-Mo carbides to Mo-V carbides. *Wei et al.* [24] measured a trapping energy of 55.8 kJ/mol associated with TiC precipitates, while *Rousseau et al.* [4] obtained a trapping energy of 17 kJ/mol corresponding to B2-NiAl coherent precipitates. These significant differences are partly linked to the coherency of the

precipitates/matrix interface [4,24,25], as semi-coherent and incoherent interfaces have an important hydrogen trapping ability, either in surface vacancies or in GNDs. Hydrogen can also be trapped in the structural vacancies found inside the precipitates, leading to high trapping energies, in the range 45-60 kJ/mol [26,27]. Finally, hydrogen trapping occurs in the elastic field created by the (semi)coherent precipitates. However, the associated trapping energies are low, *Wei et al.* [24] estimated that such energies are not higher than few kJ/mol for stresses as high as 3000 MPa. The PH13-8Mo alloy studied in this work is strengthened by nano-scale B2-NiAl precipitates that are coherent with the matrix [28–30]

Finally, the presence of a secondary austenitic phase must be taken into account, as it can also significantly affect hydrogen diffusion and trapping [31,32]. The austenite can either be residual (ie not transformed into martensite during quenching) or reverted (ie formed during the ageing treatment), the latter being found as very thin films located in between martensitic laths [28,33,34]. This morphology of austenite is believed to have an even stronger influence on hydrogen diffusion and trapping [35]. While it has been evidenced that hydrogen can be stored in the lattice of austenite [36], several studies suggest that the most impacting trapping site for hydrogen is the interface between austenite and the martensitic matrix [37–40].

Table. 1. presents data from the literature concerning hydrogen binding/trapping energies attributed to the microstructural features previously mentioned. These values are mainly obtained using electrochemical permeation and Thermal-Desorption Spectroscopy (TDS) as well as calculation (Ab-initio, Density Functional Theory). A significant scattering among and between the values of E_B and E_T can be observed, which illustrates the difficulties encountered to isolate the effect of a single microstructural feature from the rest of the microstructure and from the experiment-related uncertainties. In particular, the TDS method using the Choo-Lee / Kissinger approach [41,42] was proved to give uncertain results when peaks partly overlap [43] and/or when the range of heating rates covered is not large enough [7]. In addition, the measurement might be impacted by inhomogeneous initial hydrogen charging [44], specimen thickness [45] and by any possible microstructural changes induced by the high temperatures reached during acquisition of the spectrum. On the other hand, the electrochemical permeation technique also suffers some difficulties. The measurement can be impacted by electrochemical instabilities [46] and by surface layers (oxide layer or palladium deposition on the entry and/or exit side) [47]. In addition, determination of trap energies and trap densities requires numerous permeation experiments at different hydrogen fugacities [48] and/or temperatures [9]. Considering the uncertainties and experimental difficulties associated with both TDS and permeation, comparison of experimental results (trap densities, trap energies) obtained using both methods on the same material may allow more reliable results [18,49].

Confrontations between experimental and numerical approaches are a relevant way to strengthen the results [12,45,50–52]. This is particularly true for permeation where addressing multiple trapping using analytical approaches (such as the Kumnick and Johnson approach [48]) is not an easy matter. In most cases, homogenized models are used, where an elementary volume is characterized by a trap density and local hydrogen concentrations (both lattice and trapped hydrogen). Those models can be based on rate equations of hydrogen trapping and detrapping [45,53–56], or on the assumption of local equilibrium between lattice and trapped hydrogen I the elementary volume [57–63]. Some authors [55,64] argued that local equilibrium is achieved provided the trapping/detrapping reaction times are short compared to the long range diffusion time, which is usually the case if the specimens are thick enough. Models have been applied to the simulation of TDS spectra [45,54,58,59,61,63] and more occasionally permeation curves [12,57,62,65]. One of the limitation of such models is the number of input parameters needed, and the possibility of having several sets of parameters giving the same result. Therefore, a sufficient amount of experimental measurements

obtained in different conditions is usually needed to extract reliable parameters from the comparison between experiments and simulations. In addition, such approaches have to be complemented by a deep investigation of microstructure in order to identify and quantify the possible hydrogen traps in the material.

The objective of this study is to assess the trapping energies and trap densities associated to key microstructural features of PH13-8Mo, a widely used maraging stainless steel. In order to identify the effect of those microstructural features on the hydrogen behaviour, three metallurgical states of PH13-8Mo were studied. The microstructure of each metallurgical state was deeply characterised, with a special focus on the strengthening precipitates and austenitic phase. Several approaches were used to study the hydrogen behaviour: electrochemical permeation, thermal desorption, and numerical simulation of permeation based on a local equilibrium model. The complementarity and confrontation of results are meant to increase the accuracy and reliability of the proposed links between trapping phenomena and PH13-8Mo microstructure.

Table. 1. Literature review of hydrogen trapping energies (E_T) and binding energies (E_B) corresponding to different microstructural features in iron and steels. The lattice diffusion activation energy (E_a) has been reported to be 3-18 kJ/mol [4,18,24,41,66–68].

Trapping element	E_T **(kJ/mol)**	E_B **(kJ/mol)**
Grain boundaries	17-25 [15,41,69] 56-60 kJ/mol [70,71]	28-47 [50,51,72,73]
Dislocation (mean)	26-34 [13,15,41,69] 52 [71]	35.7 [74]
Dislocation (core)	48-60 [4,18,23]	-
Dislocation (strain field)	28 [18]	-
Vacancy	50 [4]	55-58 [51,75,76]
Precipitate (interface)	11-15 [23,77,78] 27-35 [4,18,23,79,80] 55.8 [24]	-
Precipitate (vacancies at interface and in bulk)	45-60 [26,27,52]	-
Precipitate (strain field)	10-17 [4,18,21]	1-6 [24]

2. Materials and methods

2.1. Materials

The material is a PH13-8Mo maraging stainless steel produced and supplied by Aubert&Duval. Three samples of 15 X 15 X 90 mm were solution annealed at 930°C during 1h then water quenched to obtain a martensitic structure with very little residual austenite. Two solutions annealed (SA) samples were then aged to form strengthening B2-NiAl precipitates as well as reverted austenite. The H860 state corresponds to ageing at 460°C during 90 minutes, and the H1000 state corresponds to ageing at 540°C during 4 hours. The microstructures of the SA, H860 and H1000 states were then characterised.

A model Fe-12Cr alloy was also used to measure the hydrogen diffusivity in a single-phase iron chromium BCC matrix. The alloy was produced in the laboratory and was first forged then annealed at 850°C during 4h followed by slow cooling inside the furnace to obtain a large grain size and a low dislocation density. It was used to estimate the lattice diffusivity of hydrogen in PH13-8Mo.

The chemical compositions of the studied alloys are given in *Table.* 2.

Table. 2. Chemical compositions of the studied alloys.

	Major elements (wt%)					Minor elements (wppm)			
Materials	**Fe**	**Cr**	**Ni**	**Al**	**Mo**	**C**	**O**	**S**	**N**
PH13-8Mo	Balance	12.5	8.5	0.9	2.1	341	-	4	-
Fe-12Cr	Balance	12.08	-	-	-	4	5	1	1

2.2. Microstructural analyses

For EBSD and XRD analyses, samples surface was prepared using electro-polishing in a nitric acid solution. For TEM investigations, discs with a diameter of 3 mm and a thickness of 80 µm were electropolished to perforation using a twin-jet electropolishing unit (Struers TenuPol-5) with a solution of 10% $HClO_4$ in ethanol.

EBSD was performed in a SEM ZEISS SUPRA55VP at an accelerating voltage of 20 kV. Using the EBSD data, a reconstruction algorithm [81] was used to obtain the parent austenite microstructure. This allowed us to have a good estimate of the austenitic grain size, which was not possible using conventional light microscopy observations, as chemical or electrochemical etching methods fail in clearly revealing the former austenitic grain boundaries of this material. The lath width was measured by bright field TEM observation. The total dislocation density was calculated from XRD data obtained in a diffractometer Bruker AXS D8-Advanced, using the Williamson-Hall (W-H) method [82]. The reliability of this method was confirmed by confronting its results with intra-lath dislocation density measured on bright field TEM pictures and inter-lath GND density calculated from EBSD analyses.

The B2-NiAl precipitate phase fraction was calculated using the Calphad method (Thermo-Calc software). The precipitates size was measured on dark field TEM and STEM images. The crystallography of precipitates and their coherency with the matrix were assessed using electron diffraction and their chemical nature was ensured using EDX (Energy Dispersive X-ray Spectroscopy).

The austenite content and lattice parameters of martensite and austenite were measured by XRD in a X-Ray diffractometer MDR Panalytical, using the Rietveld refinement method implemented in MAUD software. These measurements did not reveal any significant texture of the material. The austenite location was

identified in the microstructure using STEM imaging coupled with STEM-EDX mapping. Electron diffraction and bright/dark field observations were conducted at 200 kV in a TEM JEOL JEM 2011. STEM imaging and STEM-EDX mapping were performed at 200 kV in a TEM Jeol JEM-ARM200F NEO-ARM.

2.3. Electrochemical permeation

Electrochemical permeation tests were conducted in a double electrochemical cell connected to two potentiostats (Voltamaster PGP201). Saturated calomel electrodes were used as reference electrodes and platinum grids were used as counter electrodes. The tests were carried out at room temperature in a 0.1 M NaOH solution (pH 12.4). The solution was deaerated during 48h prior to first testing using nitrogen gas flow, and the deaeration was maintained during the test duration. An oxygen content of 8 ppb was measured after 48h of deaeration using an ORBISPHERE oxygen sensor.

The PH13-8Mo permeation samples were polished down to 350 µm using SiC grinding paper, then polished down to 3 µm surface state on both sides using diamond paste. The samples were welded to a nickel wire connected to the potentiostat and then rinsed with ethanol. The O-rings of the sample holder were placed in order to avoid any contact between the nickel wire and the testing solution to prevent any galvanic coupling. The exposed surface was 0.8 cm^2 on both sides.

A slightly anodic potential (open circuit potential + 50 mV) was applied to the exit surface of the sample until a stable current was obtained. Then, a strong cathodic current of -10 mA/cm^2 was applied on the entry surface during 20 minutes to remove any passive layer, followed by a constant charging current. The potential on the entry surface was monitored to ensure that it remains constant throughout the entire duration of the charging step. The rising permeation current was monitored on the exit surface until it reaches a steady state. Then, the desorption step consisted in leaving the entry surface at open circuit potential, and monitoring the decaying permeation current on the exit surface.

Charging currents ranging from -10 $\mu A/cm^2$ to -3000 $\mu A/cm^2$ were used. The changes in the shape of the permeation curves depending on the applied charging current gave information about the trapping characteristics, as presented later in this study.

2.4. Thermal Desorption Spectroscopy

Thermal Desorption Spectroscopy (TDS) tests were performed in a Jobin Yvon Horiba EMGA-621 W hydrogen analyser (TCD: Thermal Conductivity Detector). Samples of 10 X 5 X 0.5 mm were mechanically polished with SiC grinding paper down to 5 µm, cleaned with acetone and finally masked with a Mecaprex MA2 resin to proceed to one side polarization. Samples were then cathodically charged in a deaerated 1 M H_2S0_4 solution (pH = 0.18) at a constant charging current of -20 mA/cm^2. Prior to TDS measurement, the resin was removed and the sample was mechanically polished, rinsed with acetone and dried with air. The sample was then placed in a graphite crucible which was introduced in the furnace chamber. The small size of the chamber allows a purging cycle of few minutes only, resulting in little hydrogen being lost during the process. The sample was induction heated to the desired temperature at the desired heating rate, and the hydrogen flux was monitored to obtain the TDS spectrum. For each TDS test, an identical test with an empty crucible was performed to obtain a reference TDS spectrum. The reference spectrum was then subtracted from the experimental spectrum.

Specimens of the three metallurgical states were cathodically charged for different durations up to 72h. The total hydrogen content was then measured by TDS using direct heating to 2000°C. We found that the hydrogen content reaches a plateau after 48h of polarisation for the three metallurgical states. Specimens where then cathodically charged during a fixed time of 48h. TDS analyses from 80 °C to 2000 °C at specific heating rates in the range from 75 to 230 K/min were conducted to obtain the TDS spectra. The changes in TDS spectra shape depending on heating rate gave access to the trapping energies, as presented later in this study.

2.5. Simulation of permeation tests

The permeation tests were simulated using a 1D finite element model, based on local equilibrium between lattice hydrogen and trapped hydrogen, which is represented in *Fig.* 2. This model takes into account the effect of trap densities and trap binding energies. It can operate with several types of traps *i*, each one characterised by a trap density N_{Ti} and a trap binding energy E_{Bi}. In this study we used a model with two traps only, in order to keep the number of input variables reasonable, and because a three-trap model did not improve the agreement between the experimental and the simulated permeation curves.

The sample thickness was divided into 1D elements. The initial condition is a null hydrogen concentration in all elements. Boundary conditions are then applied. A constant lattice hydrogen concentration $C_{0,lattice}$ is imposed in the first element (entry surface), to be representative of the constant charging potential on the entry surface during permeation tests (surface equilibrium is supposed to be rapidly established). A null lattice hydrogen concentration is imposed in the last element (exit surface), as we suppose that all hydrogen on the exit surface is quickly oxidised by the anodic potential, which is a necessary condition for the thick membrane hypothesis. These boundary conditions are maintained throughout the charging step. Then, the lattice hydrogen concentration is set to zero in the first element in order to simulate the desorption step, as the hydrogen concentration on the entry surface is supposed to quickly drop to zero once the charging stops [83].

At each time step, the total hydrogen concentration C_{total} in each element is calculated using the Fick law (Eq. (2)) with a lattice diffusivity $D_{lattice}$, considering that only lattice hydrogen is mobile.

$$\frac{\partial C_{total}}{\partial t} = D_{lattice} \cdot \frac{\partial^2 C_{lattice}}{\partial^2 x} \qquad (2)$$

Then, lattice hydrogen and trapped hydrogen are equilibrated in each element, considering that this equilibrium is reached very quickly compared to long range diffusion kinetics [60]. This hypothesis leads to the formulation of equation (3), which links a hydrogen concentration C_{Ti} in trap *i* to the lattice hydrogen concentration $C_{lattice}$, the lattice sites density N_L, and the trap characteristics N_{Ti} and E_{Bi}, according to early works based on Fermi-Dirac statistics [60,84,85]. Equation (3) is applied for each type of trap implemented in the model.

$$C_{Ti} = \frac{N_{Ti}}{\left(1 + \frac{N_L}{C_{lattice} \cdot exp[-E_{Bi}/RT]}\right)} \qquad (3)$$

The conservation of mass is ensured in each element using equation (4).

$$C_{lattice} + \sum_i C_{Ti} = C_{total} \quad (4)$$

At each calculation step, equation (2) provides the total hydrogen concentration profile $C_{total}(t+dt,x)$ from the previous lattice hydrogen concentration profile $C_{lattice}(t,x)$. Then, once $C_{total}(t+dt,x)$ is known, the model proceeds with equilibration in every element in order to determine $C_{Ti}(t+dt,x)$ (for each type of traps) and $C_{lattice}(t+dt,x)$. Once $C_{lattice}(t+dt,x)$ is obtained, the model can proceed with the new calculation step. Equilibration is obtained in each element using equations (3) and (4) and needs the resolution of a system of N+1 equations, where N is the number of different types of traps, as presented in *Fig.* 2. However, the mathematical solution is not unique for a model simulating more than one trap. To overcome this difficulty, the correct solutions were pre-calculated and stored in a correspondence table, following the approach used by *Yaktiti et al.* [86]. This table contains values of $C_{lattice}$ covering the range of interest [0, $C_{0,lattice}$], and the corresponding values of C_{total} and C_{Ti}, that were obtained simply from equations (3) and (4). For any given value of C_{total}, it is then easy to extract the corresponding value of $C_{lattice}$ from the pre-calculated table, using linear interpolation.

Finally, the model can provide both the permeation curve (*ie* the time dependant hydrogen flux entering the last element) and the concentration profiles at a given time for each hydrogen population (lattice and trapped), from which we can deduce the trap occupancy profiles.

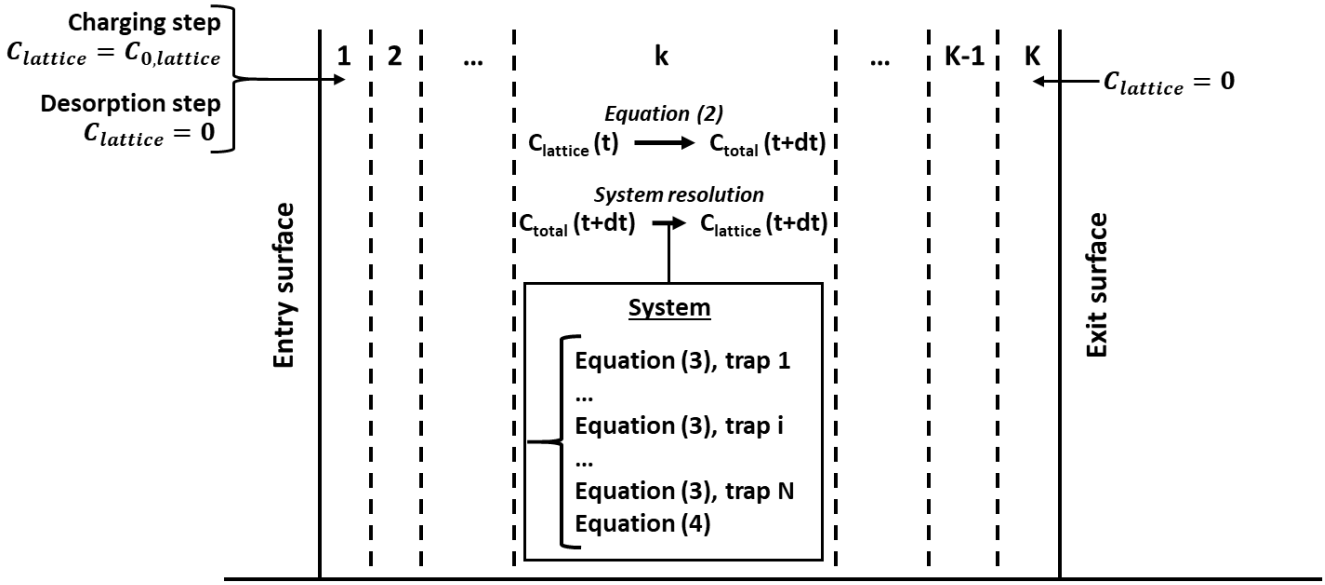

Fig. 2. Schematic representation of the 1D finite element model used to simulate permeation tests in a multi-trap material.

3. Results

3.1. Microstructure

Fig. 3 (a) and (b) show an EBSD orientation map of PH13-8Mo (H1000) and a parent phase reconstruction of this map. Such reconstructions allowed a good estimation of the former austenitic grain size, which was found to be 25 µm. This value is constant among all metallurgical states, as the ageing treatments are not performed at temperatures/durations high enough to induce any grain coarsening. *Fig. 3* (c) presents a TEM bright field observation of the lath martensite of PH13-8Mo (H1000), a mean lath width of 400 nm was measured in the material.

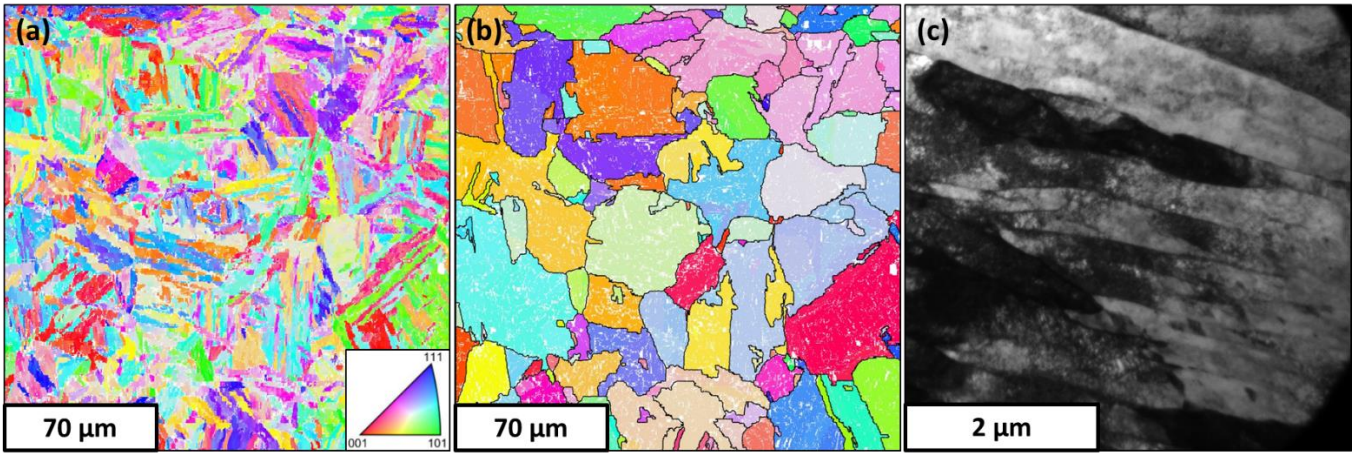

Fig. 3. EBSD analysis of PH13-8Mo (H1000): (a) Orientation map (IPFz, z being normal to the analysed surface) and (b) orientation map of the reconstructed austenite microstructure (IPFz). (c) TEM bright field observation of the lath martensite in PH13-8Mo (H1000).

Fig. 4 shows the austenite content, hardness and dislocation density measured in the three metallurgical states of the material. The austenite content increases continuously with increasing aging temperature, as a consequence of austenite reversion which is favoured at higher temperature. Hardness is similar between the two aged materials, but significantly higher in the aged states than in the SA state. Dislocation density is high (about $5x10^{14}$ m^{-2}) and is similar among the three metallurgical states. This shows that no significant dislocation annihilation occurred during the ageing treatments conducted in this study. The important increase in hardness between SA on one hand and H860 and H1000 states on the other hand is caused by the precipitation of the intermetallic phase B2-NiAl. The similar hardness observed in H860 and H1000 states suggests that the precipitation state is not very different in the two cases. This observation is consistent with previous studies which highlighted the low sensitivity of these precipitates to ageing [28–30].

Austenite content, dislocation density and hardness are summarised in *Table.* 3, along with the NiAl precipitate volume fractions. These volume fractions were estimated at equilibrium using the ThermoCalc software. It confirms that the NiAl phase fraction is close between the H860 and the H1000 states.

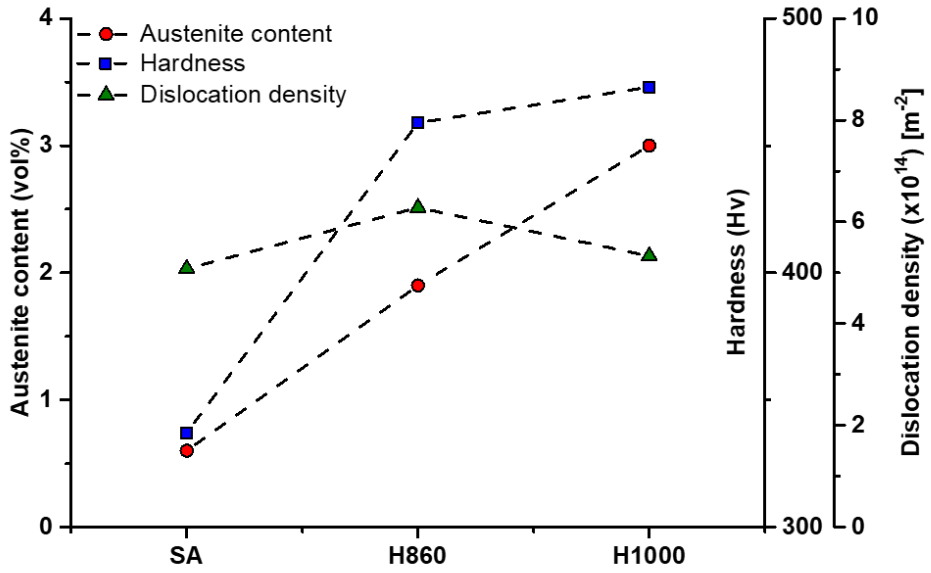

Fig. 4. Measurements of austenite content (XRD), hardness (Hv) and dislocation density (XRD) in the studied materials.

Table. 3. Austenite content, hardness, dislocation density and NiAl phase fraction measured among the three metallurgical states of PH13-8Mo. The NiAl phase fraction was obtained using ThermoCalc.

Metallurgical state	Austenite content (vol%)	Hardness (Hv)	Dislocation density [m^{-2}]	NiAl phase fraction (vol%)
Solution Annealed	0.6	337	$5.1x10^{14}$	-
H860	1.9	460	$6.3x10^{14}$	6
H1000	3.0	473	$5.3x10^{14}$	4.8

Austenite distribution in the H1000 state has been investigated using STEM and EDX (see *Fig. 5*). It appears to be present in the microstructure as thin layers on the martensitic lath boundaries and as islands both inside the laths and on lath boundaries. These observations are similar to what can be found in the literature [4,28,34,87]. The EDX profiles in Fig. 5 (c) and (d) reveal that both intra-lath and inter-lath islands display a Ni enrichment in the periphery of the island, while the Ni signal intensity is similar between the centre of the island and the martensitic matrix. It is supposed that the Ni-rich austenite corresponds to the reverted austenite, Ni being a γ-forming element with a lower solubility in the martensitic phase compared to the austenitic phase [88]. On the other hand, the retained austenite keeps its initial composition, corresponding to the nominal alloy composition. Thus, the retained austenite should have a Ni content close from the one of the martensitic matrix. Therefore, the islands of austenite should correspond to retained austenite, which was then covered by reverted austenite during ageing. The reverted austenite also formed as thin layers on lath boundaries, as can be seen on Fig. 5 (b) and (e), where a similar enrichment in Ni is identified along a lath boundary.

The thickness of the reverted austenite layers was roughly estimated to be about 10 nm in the H1000 state. As mentioned before, a mean martensitic lath width of 400 nm was measured, which would lead to a martensitic interface density of $\frac{1}{400} = 2.5 \cdot 10^6\ m^2/m^3$. Considering the 3 vol% austenite content measured in the H1000 material, a homogeneous repartition of reverted austenite on all martensitic interfaces would lead to austenite layers of thickness 12 nm, which is consistent with our observations. Thus, it is likely that austenite reversion occurred quite homogeneously on all martensitic interfaces.

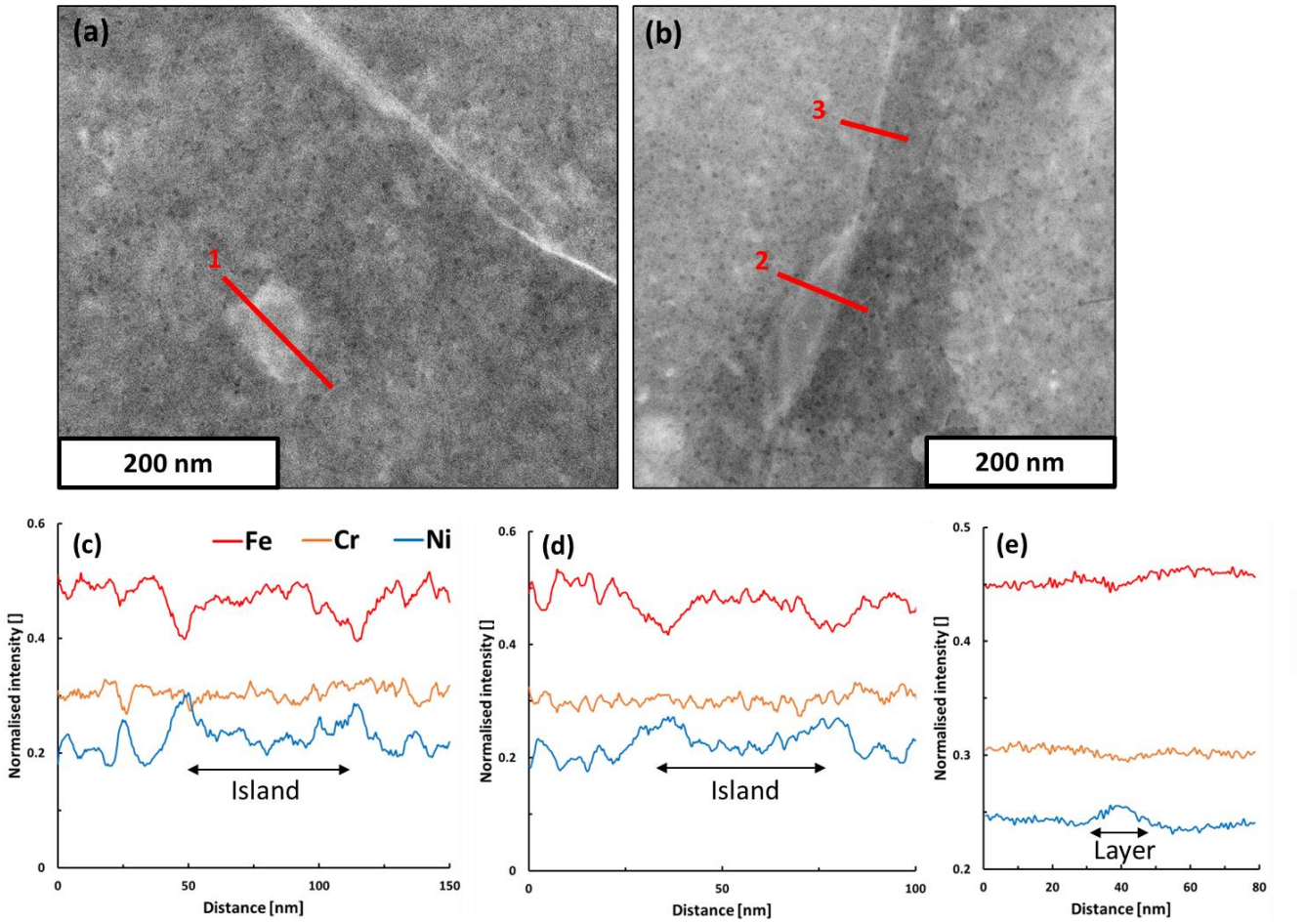

Fig. 5. STEM observations of PH13-8Mo (H1000). EDX analyses of: (c) intra-lath austenite island corresponding to line 1, (d) inter-lath austenite island corresponding to line 2, and (d) inter-lath austenite layer corresponding to line 3.

Fig. 6 shows TEM analysis of B2-NiAl precipitates in the H1000 state. Diffraction analysis was conducted with a [001] zone axis and reveals the presence of two superposed diffraction patterns as shown in *Fig.* 6 (a). The primary pattern corresponds to the BCC matrix. The secondary pattern corresponds to the NiAl precipitates, which aligns with the matrix pattern. However, the NiAl phase has a B2 superlattice structure, which results in supplementary diffraction spots on the secondary pattern. The matrix lattice parameter has been measured to be $a_M = 2.87$ Å using XRD, so that the distances in the electron diffraction pattern can be calibrated. Thus, it is possible to calculate the B2-NiAl lattice parameter from the electron diffraction patterns. A value of 2.88±0.06 Å was obtained, resulting in lattice parameter mismatch of $\delta = 0.7 \pm 2\%$ with the BCC matrix. It is to be noted that the mismatch obtained is below the measurement error. Nevertheless, this low mismatch value is in accordance with literature data [4,28,30,89]. *Fig.* 6 (b) shows a dark field observation corresponding to a diffraction spot belonging to the secondary diffraction pattern.

The B2-NiAl precipitates can be observed, and appear to be spherical, with a diameter of about 8 nm. It also seems that the precipitates are evenly distributed in the matrix.

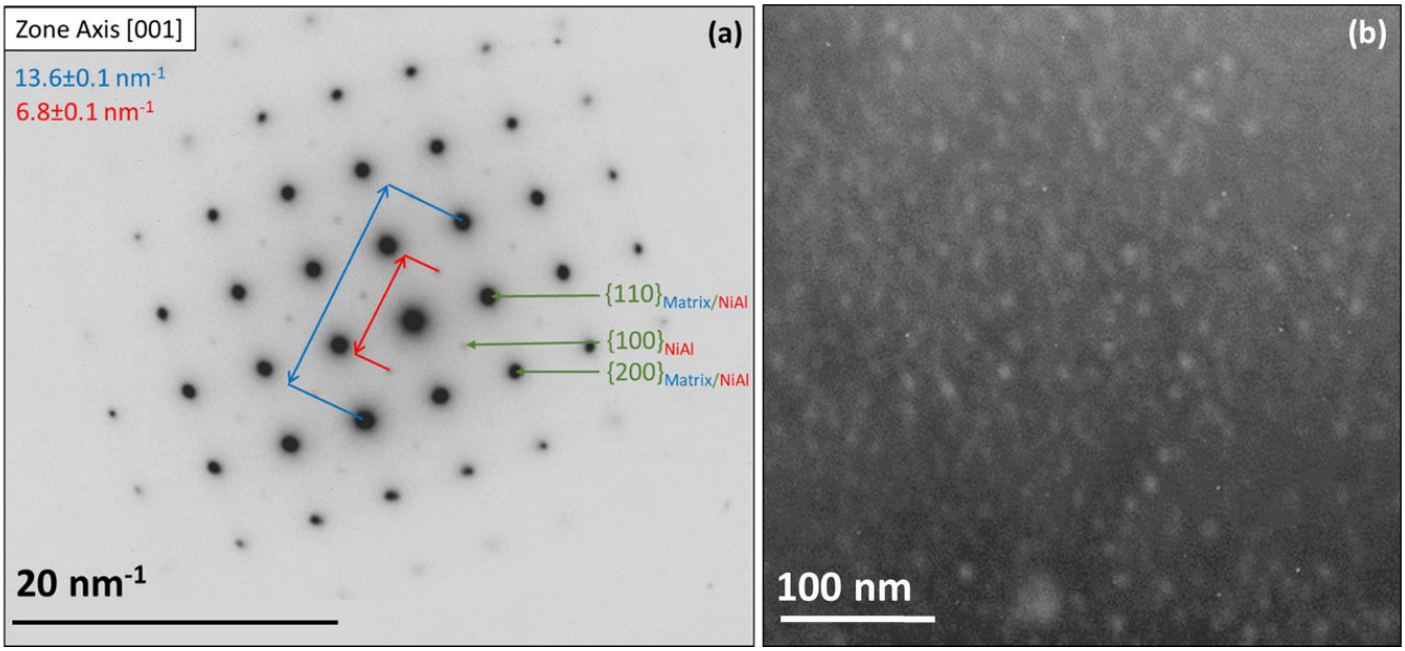

Fig. 6. TEM analysis of PH13-8Mo (H1000). (a) diffraction patterns of the BCC matrix and the B2-NiAl precipitates. (b) dark field observation of the B2-NiAl precipitates.

Fig. 7 shows a STEM observation of the nano-scale precipitates as well as an EDX profile obtained across one of them. STEM observations confirm that the precipitates are spherical, with a diameter of about 8 nm. As expected, EDX profile reveals an enrichment in Ni and Al when the electron beam intersects with the precipitate. The dark dots on STEM observations, corresponding to B2-NiAl precipitates, can be seen in *Fig. 5* (a) and (b) as well, where it can also be observed that the precipitates did not form inside the austenitic phase.

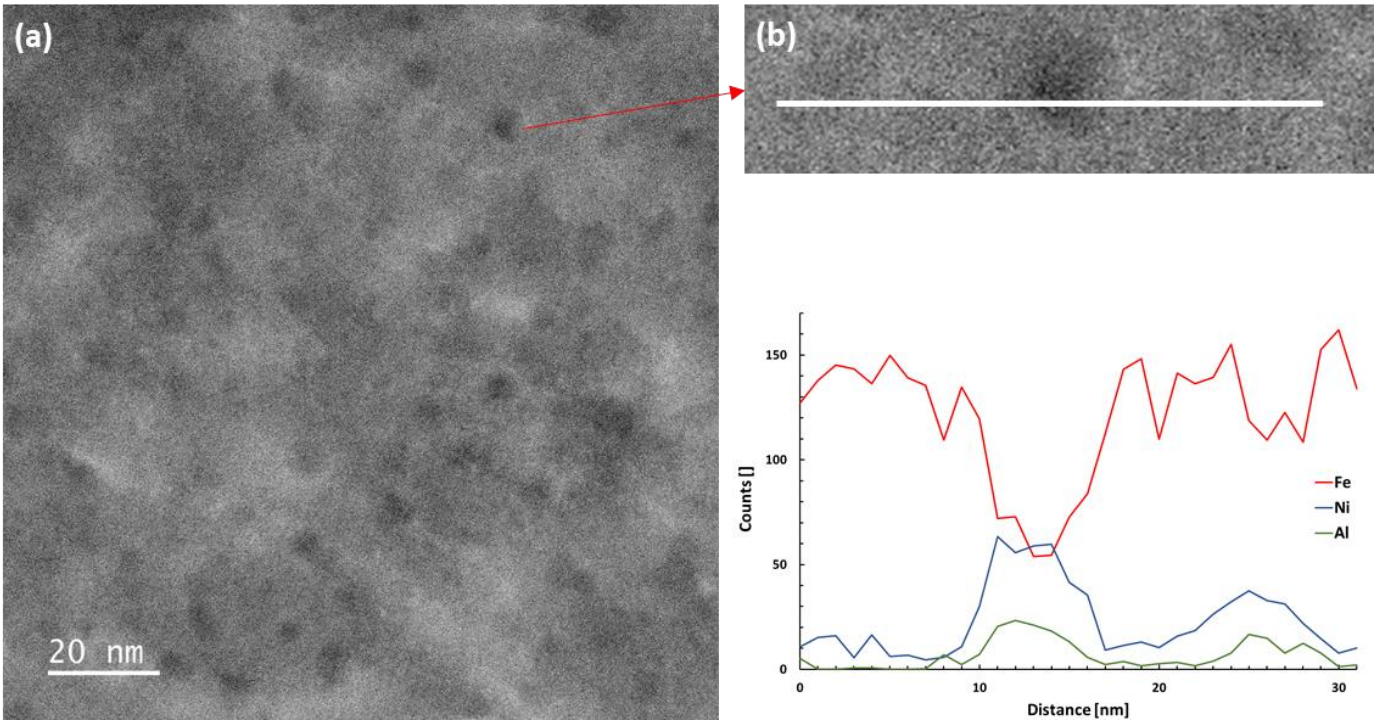

Fig. 7. STEM observations of PH13-8Mo (H1000). (a) STEM observation of precipitates and (b) EDX profile showing a significant increase in Ni and Al when crossing a precipitate.

The TEM dark field and STEM observations of B2-NiAl precipitates revealed that the precipitates are spherical, with a diameter of about 8 nm and are homogeneously distributed in the matrix. Considering the precipitates small size and the low lattice parameter mismatch at the precipitates/matrix interface, the B2-NiAl precipitates are supposed to be coherent with the matrix, as suggested by several studies [4,28,30,89]. A simple geometrical criterion (equation (5)) proposed by Brooks [90] suggests that an interface remains coherent as long as no interfacial dislocation is able to form, which is the case if

$$l \cdot \delta \leq b \qquad (5)$$

with l the interface length, δ the lattice parameter mismatch at the interface and b the burger vector of an interface dislocation. In our case, the B2-NiAl precipitates should start to lose their coherency with the matrix when reaching a diameter of about 40 nm, which is significantly above the precipitate size observed here. Hence, the B2-NiAl precipitates present in the studied material remain coherent with the matrix and should not generate interfacial dislocations.

3.2. Hydrogen electrochemical permeation

Fig. 8 (a), (b) and (c) show the rising transients of permeation tests performed on the three metallurgical states using different charging currents. The permeation curves appear to be strongly impacted by the changes in charging current as well as by the metallurgical state of the material. Two values seem to be particularly impacted, the steady state permeation current (J_{SS}), and the hydrogen exit time (t_{exp}) defined as the duration required to reach 1% of J_{SS}. It can be seen that the hydrogen exit times are much shorter for the solution annealed state than for the aged states. *Fig.* 8 (d) and (e) show the variation of steady state permeation current (J_{ss}) and exit time respectively with the charging current. As expected, the steady state current tends to increase with increasing charging current, although some experimental scattering is visible. Additionally, it is observed that the hydrogen exit time tends to decrease with increasing charging current.

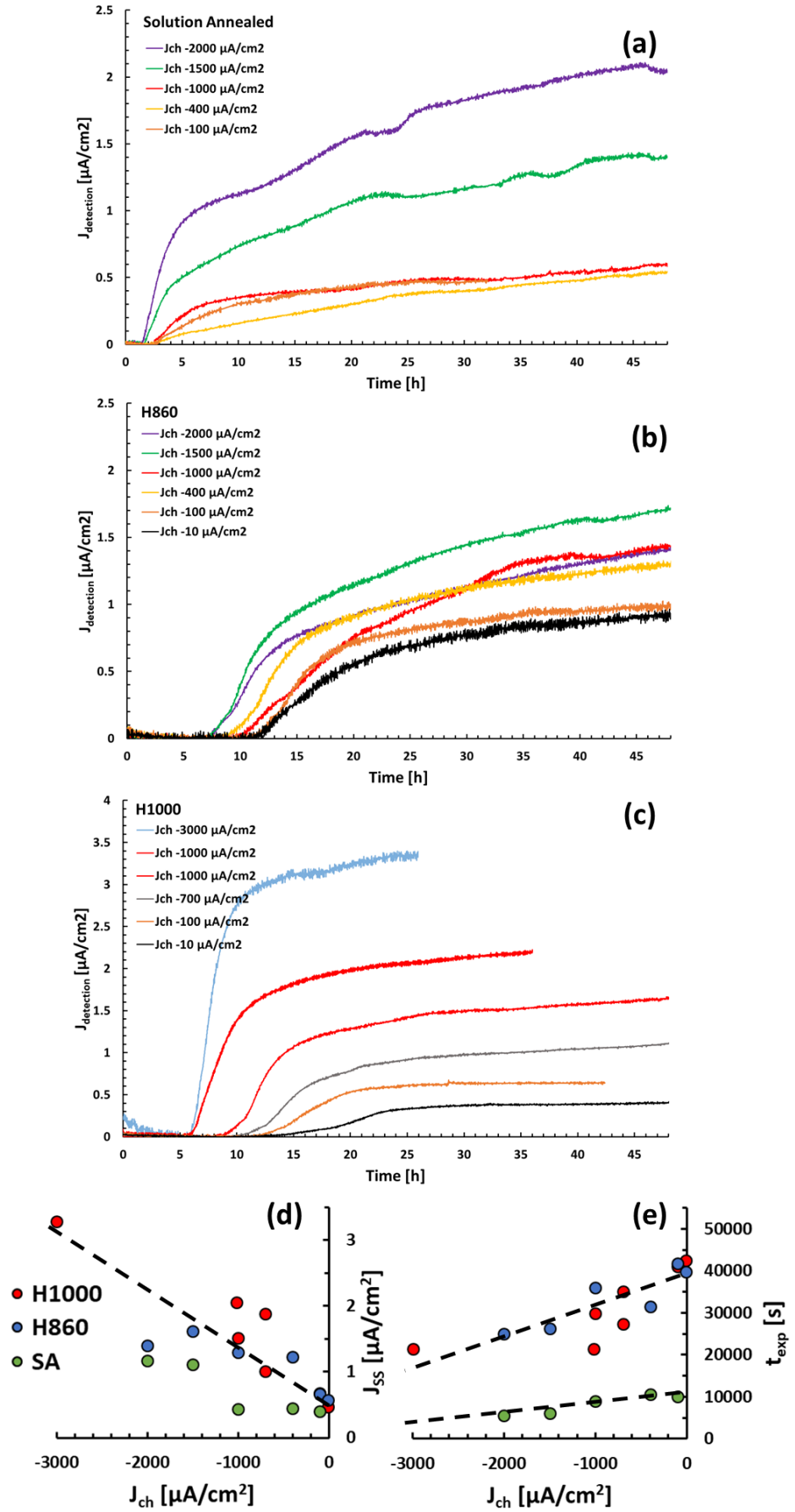

Fig. 8. Influence of charging current on permeation curves: (a) SA state, (b) H860 state and (c) H1000 state. (d) shows the relation between the permeation current in stationary state J_{SS} and the charging current. (e) shows the relation between the hydrogen exit time t_{exp} (time at 1% of J_{SS}) and the charging current.

The link between the hydrogen exit time and the steady state permeation current has been studied by Kumnick & Johnson [48]. The authors established an analytical solution for the hydrogen exit time in a material containing a single trap population, derived from a more general model proposed by McNabb and Foster [56]. This analytical solution depends on the trap characteristics (binding energy and trap site density) and the charging conditions.

$$t_{exp} = t_{lattice}\left\{1 + \frac{3\alpha}{\beta} + \frac{6\alpha}{\beta^2} - \frac{6\alpha}{\beta^3}(1+\beta)ln(1+\beta)\right\} \quad (6)$$

$$\alpha = \frac{N_T}{N_L} exp\left(\frac{E_B}{RT}\right) \quad (7)$$

$$\beta = \frac{C_{0,lattice}}{N_L} exp\left(\frac{E_B}{RT}\right) \quad (8)$$

Where t_{exp} and $t_{lattice}$ are the hydrogen exit times respectively with and without trapping, N_T and N_L are the trap site and lattice site densities respectively, E_B is the trap binding energy, and $C_{0,lattice}$ is the lattice hydrogen concentration close to the charging surface of the sample.

Equation (6) can be simplified in conditions where $C_{0,lattice}$ is either sufficiently high (regime of nearly saturated traps) or sufficiently low (regime of low trap occupancy). Then, equation (6) can be written as equation (9) or equation (10).

Nearly saturated traps $$\frac{t_{exp}}{t_{lattice}} = 1 + \frac{3\alpha}{\beta} = 1 + \frac{3N_T}{C_{0,lattice}} \quad (9)$$

Low trap occupancy $$\frac{t_{exp}}{t_{lattice}} = 1 + \alpha = 1 + \frac{N_T}{N_L} exp\left(\frac{E_B}{RT}\right) \quad (10)$$

As a consequence, in the regime of nearly saturated traps, $\frac{t_{exp}}{t_{lattice}}$ and $\frac{3}{C_{0,lattice}}$ display a linear relationship with a slope of N_T. This approach is frequently used to estimate hydrogen trap density in metallic materials using permeation tests [91,92].

In the regime of low trap occupancy, $\frac{t_{exp}}{t_{lattice}}$ does not depend on $C_{0,lattice}$, and the binding energy E_B can be calculated if N_T and N_L are known. In this study we considered $N_L = 5.08 \cdot 10^{29}\ m^{-3}$, which is the density of tetrahedral interstitial sites in the studied material, as hydrogen is believed to occupy tetrahedral position in BCC structures [24,67,93].

The hydrogen exit time without trapping can be calculated as:

$$t_{lattice} = \frac{e^2}{25 \cdot D_{lattice}} \quad (11)$$

where e is the sample thickness, and $D_{lattice}$ is the lattice diffusivity of hydrogen. We remind that the exit time is defined here as the time needed to reach 1% of the steady state current.

From the steady state permeation current observed on a given permeation curve, the lattice hydrogen concentration close to the charging surface of the sample can be calculated as:

$$C_{0,lattice} = \frac{J_{SS} \cdot e \cdot N_a}{D_{lattice} \cdot F} \quad (12)$$

With N_a the Avogadro number and F the Faraday constant. It can be seen that the value of $D_{lattice}$ must be assessed to be able to calculate the values of $t_{lattice}$ and $C_{0,lattice}$. In the literature, the lattice diffusion of hydrogen in pure iron has been widely studied and a large scatter of the diffusivity values was obtained [67,77,92]. Hydrogen lattice diffusivity seems to be strongly dependant on the iron purity [94]. Thus, in our case the presence of alloying elements is suspected to have a strong effect on hydrogen lattice diffusivity.

In this work, our approach to estimate $D_{lattice}$ was to conduct a permeation test on the pure iron-chromium reference alloy presented earlier (see composition in *Table.* 2). The study of this very pure model alloy allows us to take into account the effect of chromium on the lattice diffusivity of hydrogen. The same chromium content as PH13-8Mo was chosen for the reference material. However, it was not possible to include nickel and molybdenum, since the addition of these elements would make it impossible to obtain a single phase BCC alloy. The reference Fe-12Cr alloy was annealed at high temperature (850°C/4h) in order to minimize the density of defects. The hydrogen diffusion coefficient measured on that alloy using electrochemical permeation (see Appendix) was $1 \cdot 10^{-10}$ m^2/s, which will be used as $D_{lattice}$ in this study.

Increasing the charging current during permeation tests should result in an increase in $C_{0,lattice}$ considering equation (12). Using the permeation tests at different charging currents, leading to different values of $C_{0,lattice}$, the Kumnick & Johnson method was applied to the studied materials, and the results are shown in *Fig.* 9.

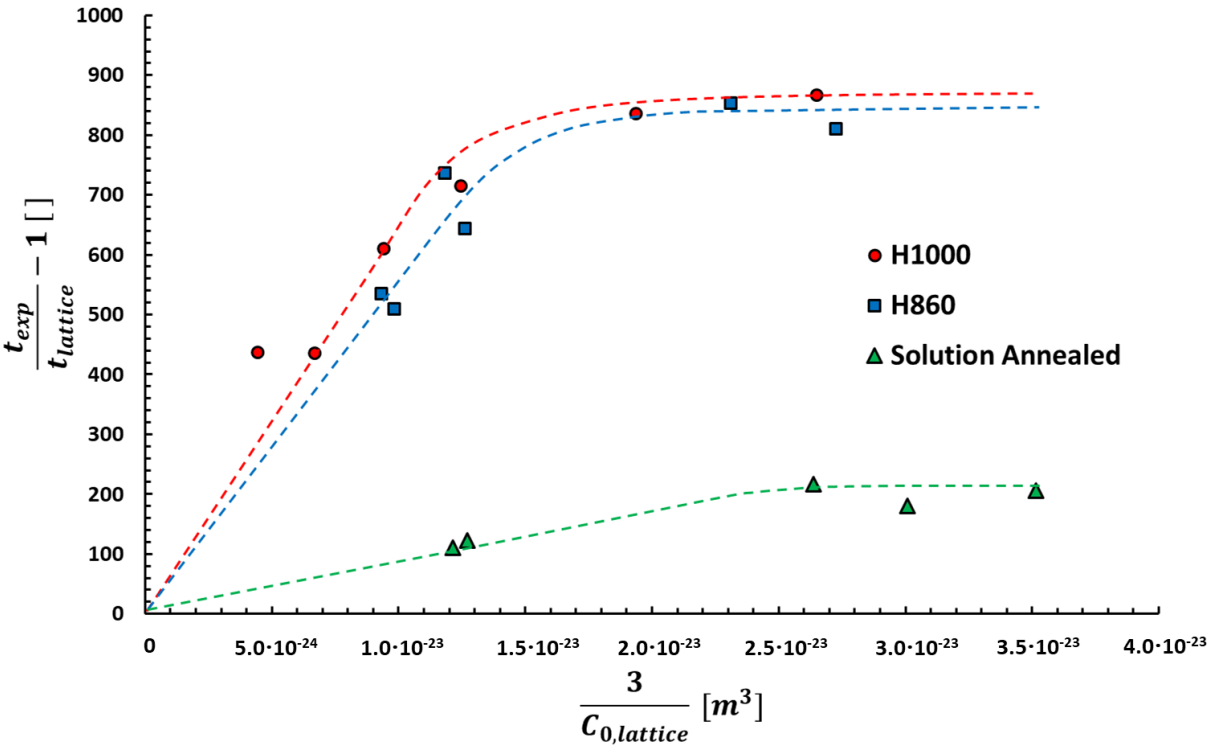

Fig. 9. Application of the Kumnick & Johnson method to the studied materials.

In *Fig.* 9 it can be observed a similar shape of the curves corresponding to the three metallurgical states. The first part of the curves has a linear shape. This part corresponds to the high $C_{0,lattice}$ values, for which the traps are partially or totally saturated. The slope of this part of the curves is equal to the total trap density N_T (equation (9)). For smaller values of $C_{0,lattice}$, i.e. higher values of $\frac{3}{C_{0,lattice}}$, a plateau is observed. Knowing the value of this plateau and the trap density previously calculated, it is possible to calculate the trap binding energy E_B (equation (10)). This value of binding energy is a "mean" of the energies of all traps present in the material, as the Kumnick & Johnson method supposes the presence of only one type of traps with the same binding energy. The values of N_T and E_B obtained by this method are summarised in *Table.* 4.

Table. 4. Total trap density and mean trap binding energy found in the three metallurgical states by applying the Kumnick & Johnson method with the data obtained from permeation tests at different charging currents.

Metallurgical state	Total trap density [m^{-3}]	Mean trap binding energy [kJ/mol]
Solution Annealed	$8.6x10^{24}$	40.5
H860	$5.6x10^{25}$	39.5
H1000	$6.5x10^{25}$	39.2

It can be seen that a significant increase in trap density occurs when going from the SA state to the H860 state. However, the two aged states display similar trap densities. The trap densities found are in accordance with what is expected for martensitic steels [12,95]. Finally, the binding energy is similar among the three metallurgical states.

3.3. Thermal Desorption Spectroscopy

Fig. 10 (a) shows TDS spectra obtained for the three metallurgical states using a heating rate of 130 K/min. The total hydrogen concentration in the TDS sample is proportional to the area under the corresponding TDS spectrum. It appears that the aged states can store more hydrogen than the solution annealed material, and this is particularly true for the H1000 state. *Fig.* 10 (b) displays the decomposition of a TDS spectrum into four Gaussian distributions. Each peak corresponds to a hydrogen population sharing a common trapping energy. *Fig.* 10 (c) shows the hydrogen concentrations corresponding to each Gaussian peak for the three metallurgical states, these concentrations are summarised in *Table.* 5.

It can be seen that the difference in hydrogen concentration between the SA state and the H860 state is mainly attributed to the peak 3, while the difference in hydrogen concentration between the H860 state and the H1000 state is mainly attributed to the peak 2. The peak 1 concentration is identical for the three states, and the peak 4 concentration, although very low, increases continuously with the ageing temperature.

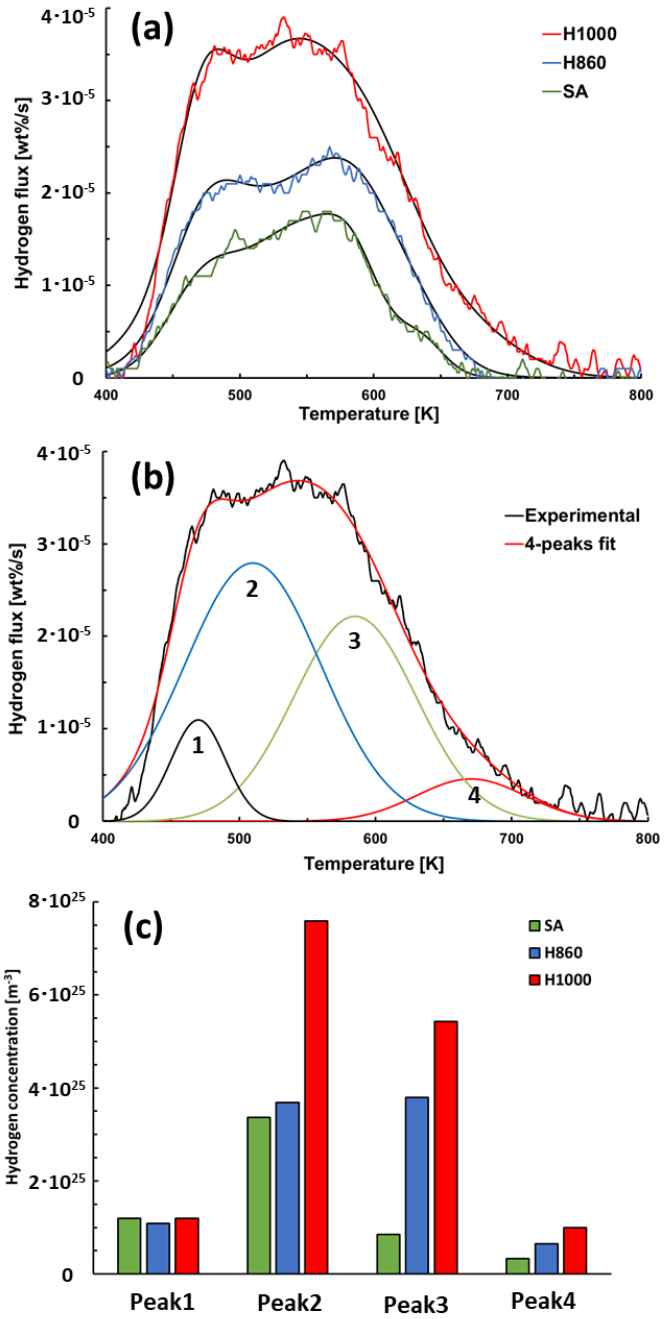

Fig. 10. (a) TDS spectra of the three materials, obtained with a heating rate of 130K/min. (b) decomposition of a TDS spectrum into four Gaussian peaks. (c) Hydrogen concentrations corresponding to each Gaussian peak for the three metallurgical states.

Table. 5. Hydrogen concentrations corresponding to the four Gaussian peaks used for the decomposition of the TDS spectra (130 K/min).

Metallurgical state	H concentration (peak 1) [m^{-3}]	H concentration (peak 2) [m^{-3}]	H concentration (peak 3) [m^{-3}]	H concentration (peak 4) [m^{-3}]
H1000	$1.2x10^{25}$	$7.6x10^{25}$	$5.4x10^{25}$	$1.0x10^{25}$
H860	$1.1x10^{25}$	$3.7x10^{25}$	$3.8x10^{25}$	$6.5x10^{24}$
SA	$1.2x10^{25}$	$3.4x10^{25}$	$8.5x10^{24}$	$3.3x10^{24}$

The trapping energies can be assessed by performing TDS tests at different heating rates. *Fig. 11* (a) displays TDS spectra of the H1000 state obtained at heating rates ranging from 130 K/min to 230 K/min. When the heating rate is increased, the TDS peaks are shifted toward higher temperatures. This phenomenon has been well established in the literature [41,96].

The trapping energy associated with a single peak can be deducted from the peak shifting relative to the heating rate, according to the Kissinger's equation [42].

$$\frac{\partial\, ln\left(\frac{\varphi}{T_p^2}\right)}{\partial\, \frac{1}{T_p}} = \frac{-E_T}{R} \qquad (13)$$

where φ is the heating rate, T_p is the peak temperature, and E_T is the associated trapping energy.

Fig. 11 (b) and (c) shows the Choo-Lee plots $ln\left(\frac{\varphi}{T_p^2}\right)$ as a function of $\frac{1}{T_p}$ [41] obtained for the two aged materials. The hydrogen concentrations obtained in the SA state were too low for this analysis to be performed accurately. From the slope of the datasets of *Fig. 11*, it is possible to calculate the trapping energies associated with each individual peak, for the two aged materials.

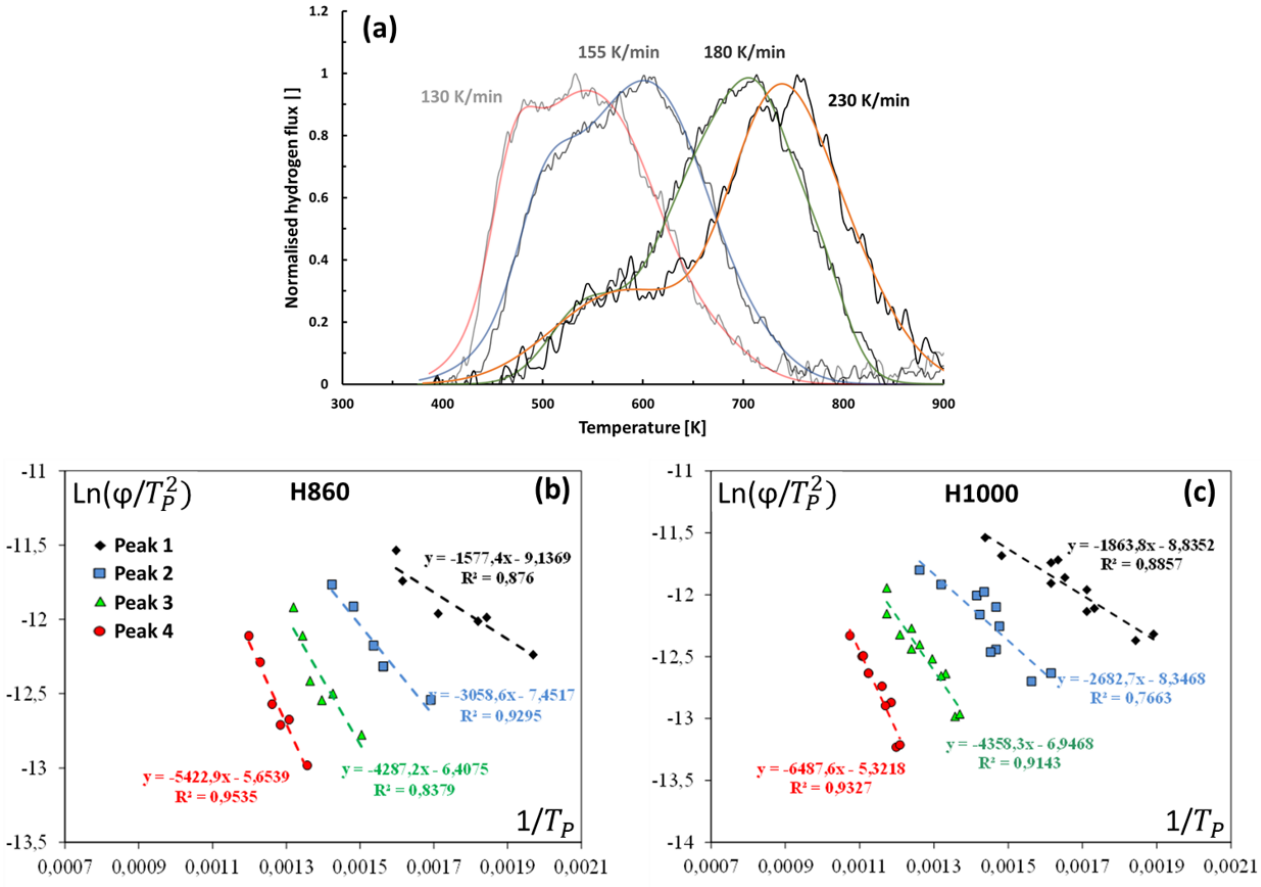

Fig. 11. (a) Effect of heating rate on the TDS spectra (H1000 state) and Choo-Lee plots obtained for the (b) H860 material and (c) H1000 material.

Four energies were calculated in H860 and H1000 materials (*Table.* 6.), and it appears that they are similar between these two materials, meaning that the materials should contain the same kind of hydrogen traps.

The first energy of 14.5 kJ/mol is the activation energy for hydrogen lattice diffusion, which is in the range of values found in the literature (see *Table.* 1). From this energy it is possible to evaluate the corresponding

lattice diffusivity using equation (14) [60], where E_a is the diffusion activation energy, λ is the distance between lattice sites, and υ is the hydrogen vibration frequency.

$$D_{lattice} = \lambda^2 \upsilon \cdot exp\left(\frac{-E_a}{RT}\right) \quad (14)$$

Nagano et al. [97] found a $\lambda^2\upsilon$ value of 4.2x10^{-8} m^2/s in pure BCC iron. Assuming that this value is similar in the PH13-8Mo steel studied here, and considering the activation energy of 14.5 kJ/mol determined from TDS, we obtained a theoretical lattice diffusivity of 1.1x10^{-10} m^2/s at room temperature. This is in excellent agreement with the diffusivity value that we measured using permeation on our reference Fe-12Cr material (10^{-10} m²/s).

The peaks numbered 2, 3 and 4 correspond to different traps. The trapping energies of peaks 2 and 3 correspond to rather reversible trapping at room temperature, and the trapping energy of peak 4 corresponds to nearly irreversible trapping according to previous studies [18].

Table. 6. Activation energy for hydrogen lattice diffusion and trapping energies found in the H1000 and H860 states by applying the Kissinger equation to the TDS spectra fitted with four Gaussian peaks.

Metallurgical state	Activation energy for H lattice diffusion (peak 1) [kJ/mol]	Trapping energy (peak2) [kJ/mol]	Trapping energy (peak3) [kJ/mol]	Trapping energy (peak4) [kJ/mol]
H1000	15.4	22.2	36.7	54
H860	13.5	25.1	35.7	45.3

3.4. Simulation of permeation tests

A numerical model of hydrogen diffusion and trapping, using 1D finite element method, was used to simulate permeation curves. Contrary to the Kumnick and Johnson analytical model presented previously, this numerical model can be used to assess the effect of several trap populations, with different binding energies and trap densities.

Fig. 12 shows an example of the effect of trap density and trap energy on the permeation curves simulated by a 1-trap model. The values of $D_{Lattice}$ and $C_{0,Lattice}$ used are 10^{-10} m^2/s and 5.0x10^{23} m^{-3} respectively. It can be seen that shallow (E_B = 20 kJ/mol, *Fig. 12* (a)) and intermediate (E_B = 35 kJ/mol, *Fig. 12* (b)) trapping has similar effects on the permeation curve. However, shallow trapping (E_B = 20 kJ/mol) only has an influence on the permeation curve when the associated trap density is above 10^{26} m^{-3} (Fig. 9 (a)), which is far higher than the trap density measured in our materials. Deep trapping (E_B = 50 kJ/mol, (*Fig. 12* (c)) has a very strong influence on the hydrogen exit time, even for a relatively low trap density. In addition, the rising transient obtained are much steeper than with shallower traps. The decay transient is also affected: on the time scale investigated here, the under-curve area is very limited for E_B = 50 kJ/mol as most of the hydrogen does not desorb. However, a very slow desorption is observed for very long times.

The simulations presented in *Fig. 12* show that the shape of the permeation curve (exit time, slope of the rising and decaying transients, under-curve area) is strongly affected by the trapping parameters introduced

into the model. Consequently, it is in principle possible to fit both the hydrogen exit time and the shape of transients of an experimental permeation curve using a multi-trap model, as shown later.

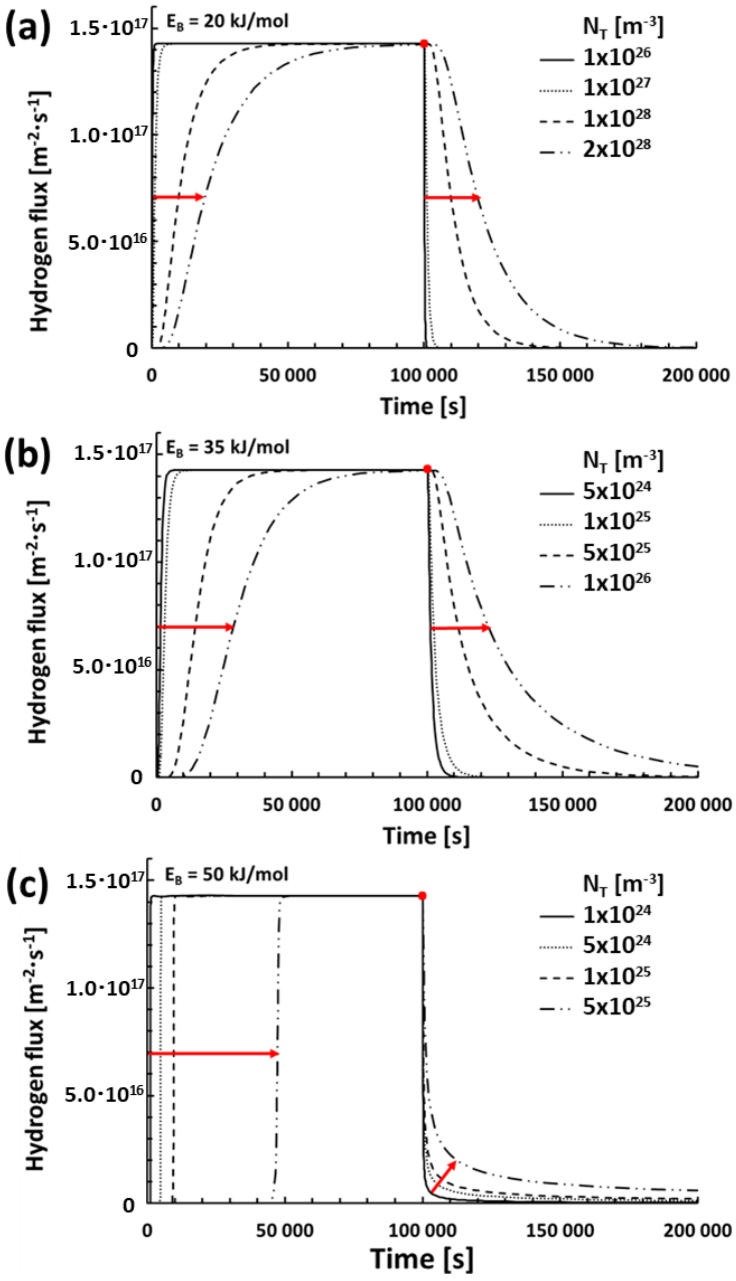

Fig. 12. Individual effect of traps of different binding energies on the simulated permeation curves ($D_{lattice}$ = 10^{-10} m^2/s, $C_{0,Lattice}$ = $5x10^{23}$ m^{-3}). (a) shallow trapping, (b) intermediate trapping, (c) deep trapping. The red dot on each curve corresponds to the beginning of the desorption step.

Hydrogen concentration profiles can also be obtained from the model. *Fig.* 13 shows examples of trap occupancy profiles during a permeation test for E_B = 20, 35 and 50 kJ/mol and N_T = 10^{25} m^{-3}. At the end of the rising transient (Fig. 13 (a)), it can be seen that the 50 kJ/mol traps are fully saturated, and that the 35 kJ/mol traps are starting to saturate as the corresponding profile is deviating from linear shape. The 20 kJ/mol traps on the other hand have a very low occupancy. At the end of the decaying transient (*Fig.* 13 (b)), the 50 kJ/mol traps are still close from saturation, which shows their nearly irreversible nature at room

temperature. The 20 kJ/mol and 35 kJ/mol traps however are reversible traps, as their occupancy diminish strongly during the decaying transient.

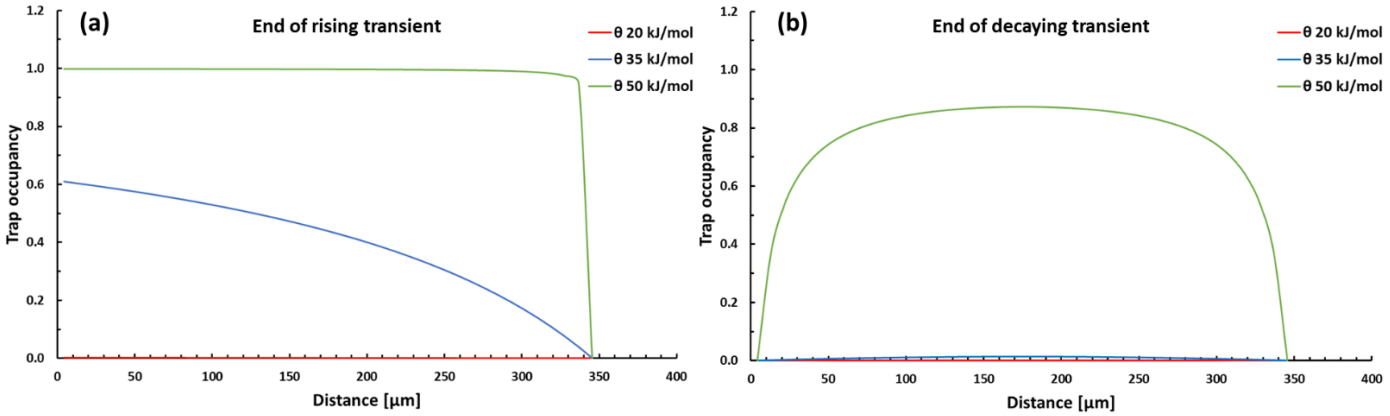

Fig. 13. Trap occupancy across the permeation sample for different binding energies, (a) at the end of rising transient and (b) at the end of decaying transient ($D_{Lattice}$ = 10^{-10} m^2/s, $C_{0,Lattice}$ = $5x10^{23}$ m^{-3}, N_T = 10^{25} m^{-3} for all traps).

In the following, some of the model input parameters were adjusted to fit the experimental permeation curves. The fitting of permeation curves was performed using a one trap and a two traps model. The input parameters are $D_{lattice}$, $C_{0,lattice}$, N_L and two parameters for each trap population (a trap density N_{Ti} and a trap binding energy E_{Bi}). In order to ensure the unicity of the set of parameters giving the best fit, some constraints were introduced:

- $D_{lattice}$ is fixed as the value measured on the reference Fe-Cr alloy (10^{-10} m^2/s),
- N_L is fixed as the density of tetrahedral interstitial sites in the BCC matrix ($5.08x10^{29}$ m^{-3}),
- $C_{0,lattice}$ is fixed as $C_{0,lattice\ (model)} = C_{0,lattice\ (experimental)} = \frac{J_{SS} \cdot e}{D_{lattice}}$, where J_{ss} is the measured hydrogen flux in the stationary regime, and e is the specimen thickness,
- N_{Ti} are constrained as $\sum N_{Ti} = N_{T\ (experimental)}$, where $N_{T(experimental)}$ is the total trap density determined from the Kumnick and Johnson analysis of the experimental data (*Fig.* 9, *Table.* 4).
- E_{Bi} can be freely varied.

An example of fits using either the one trap model or the two traps model is presented in *Fig.* 14. In all cases the total trap density is N_T = $6.5x10^{25}$ m^{-3}. In *Fig.* 14 (a), the one trap model with E_B = 37.5 kJ/mol gives the correct exit time but the shape of the transients is poorly fitted, especially that of the decaying transient. On the other hand, using E_B = 34 kJ/mol, the shape of the transients is correctly simulated but the model does not give the correct exit time. *Fig.* 14 (b) shows the results obtained using the two traps model. In this case, it is possible to find a set of parameters N_{T1}, E_{B1}, N_{T2} and E_{B2} (obeying the constraints mentioned above) so as to fit both the hydrogen exit time and the decaying transient shape.

In the example shown in *Fig.* 14, it is to be noticed that the fit of the rising transient is not as good as that of the decaying transient. This observation was made in all the fits conducted in this study. It is assumed that parasitic phenomena, such as evolution of surface oxides, may affect the shape of the experimental rising transient during the permeation test. In all the fits conducted in this study, much attention was paid to the exit time and the shape of the decaying transient, whereas the shape of the rising transient was considered less important. So the fit is considered good when the exit time is correct and the shape of the decaying transient is correctly described.

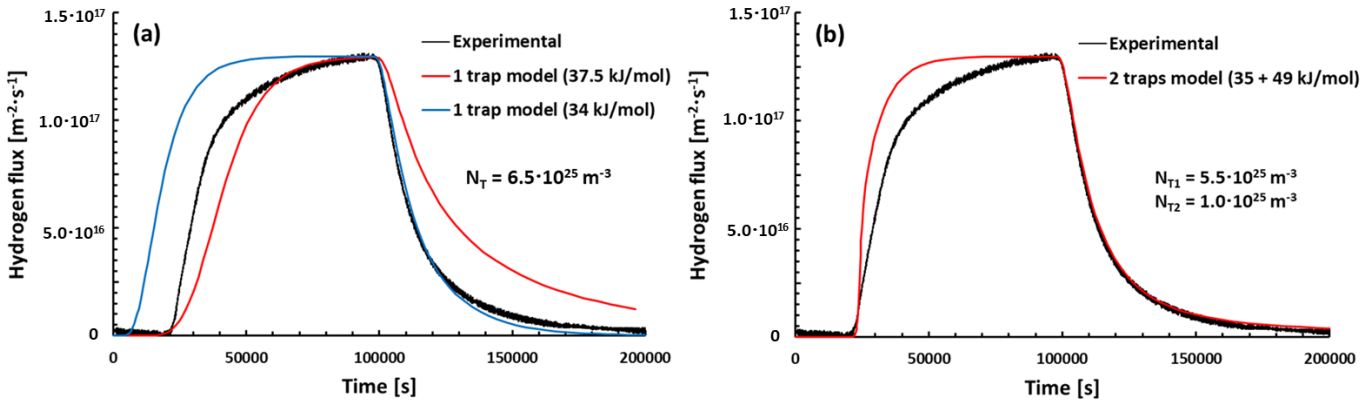

Fig. 14. Fitting of a permeation curve (H1000 state) using a model accounting for hydrogen trapping: (a) one trap model and (b) two traps model. $C_{0,lattice}$ = 4.5x10^{23} m^{-3}.

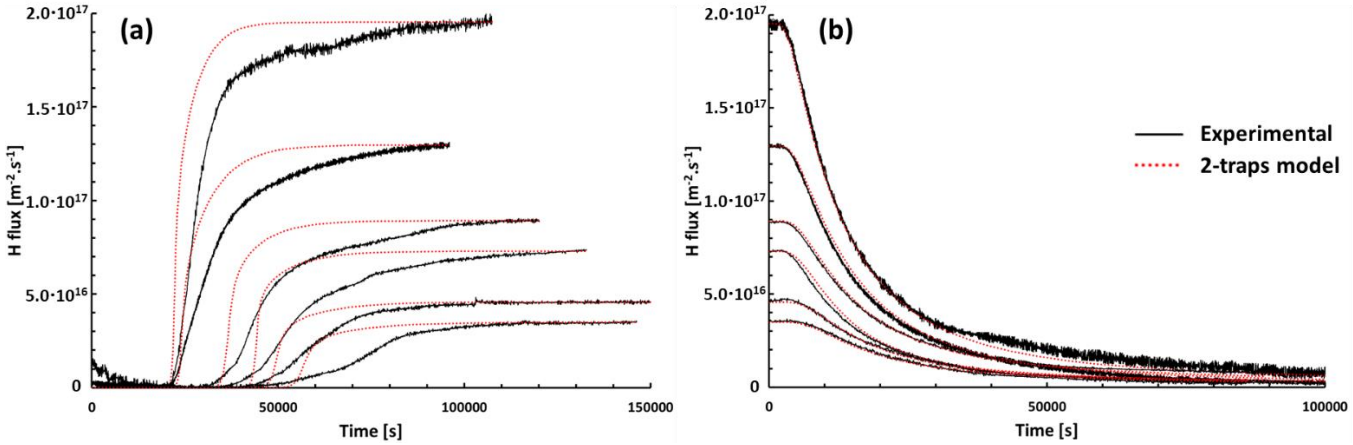

Fig. 15. Fitting of permeation curves (H1000 state) using the two traps model. (a) Rising transients and (b) decaying transients.

All the permeation curves of the three materials obtained at different charging currents were fitted using the two traps model. *Fig.* 15 presents the fits obtained for the H1000 material and *Table. 7* shows a summary of the input parameters used for the three materials in all the charging conditions tested. It is remarkable that, for a given material, the adjusted parameters N_{T1}, N_{T2}, E_{B1} and E_{B2} are practically unchanged for the different charging conditions. In other words, a whole set of permeation curves obtained on a given material can be fitted with the same material-related input parameters, i.e. by just varying the $C_{0,lattice}$ values. In addition, very close values of binding energy were found for the three metallurgical states. On the other hand, the trap densities are significantly less for the solution annealed material. In the three metallurgical states tested, there is a majority (~85%) of intermediate energy traps (~35 kJ/mol) and a minority (15%) of deep traps (~50 kJ/mol).

Table. 7. Summary of the input parameters used to fit the experimental permeation curves using the two traps model. $D_{lattice}$ is obtained from a permeation measurement on the reference Fe-Cr alloy. $C_{0,lattice}$ is obtained from equation (12) *using the steady state permeation current. N_T is taken from the Kumnick & Johnson analysis. N_{T1} and N_{T2} are constrained using $N_{T1}+ N_{T2}= N_T$. We used a value of $N_L = 5.08x10^{29}$ m^{-3} for the lattice sites concentration.*

Materials	Charging current [μA/cm²]	Fixed input values			Values adjusted with constraint		Values freely adjusted	
		$D_{lattice}$ [m²/s]	$C_{0,lattice}$ [m⁻³]	N_T [m⁻³]	N_{T1} [m⁻³]	N_{T2} [m⁻³]	E_{B1} [kJ/mol]	E_{B2} [kJ/mol]
H1000	-3000	10^{-10}	$7.2x10^{23}$	$6.5x10^{25}$	$5.2x10^{25}$	$1.3x10^{25}$	34.5	48
	-1000		$4.5x10^{23}$		$5.5x10^{25}$	$0.8x10^{25}$	34.5	48.5
	-1000		$3.2x10^{23}$		$5.3x10^{25}$	$1.3x10^{25}$	34	48
	-700		$2.4x10^{23}$		$5.5x10^{25}$	$1.2x10^{25}$	34	51
	-100		$1.6x10^{23}$		$5.7x10^{25}$	$0.9x10^{25}$	34	50
	-10		$1.2x10^{23}$		$5.9x10^{25}$	$0.8x10^{25}$	34	50
					$(5.5\pm0.3)x10^{25}$	$(1.0\pm0.2)x10^{25}$	34.2±0.3	49.3±1.3
H860	-2000		$3.2x10^{23}$	$5.6x10^{25}$	$4.6x10^{25}$	$1.0x10^{25}$	34	50
	-1500		$3.2x10^{23}$		$4.5x10^{25}$	$1.0x10^{25}$	34	48
	-1000		$2.6x10^{23}$		$4.2x10^{25}$	$1.4x10^{25}$	35	47
	-400		$2.5x10^{23}$		$4.3x10^{25}$	$1.3x10^{25}$	39.5	53
	-100		$1.5x10^{23}$		$4.7x10^{25}$	$0.9x10^{25}$	34	49
	-10		$1.2x10^{23}$		$4.9x10^{25}$	$0.7x10^{25}$	33	49
					$(4.6\pm0.2)x10^{25}$	$(1.0\pm0.2)x10^{25}$	34±0.6	48.5±1
SA	-2000		$2.3x10^{23}$	$8.6x10^{24}$	$8.0x10^{24}$	$0.6x10^{24}$	38	50
	-1500		$2.5x10^{23}$		$8.0x10^{24}$	$0.6x10^{24}$	37.5	50
	-1000		$9.8x10^{22}$		$8.1x10^{24}$	$0.5x10^{24}$	38	50
	-400		$1.1x10^{23}$		$8.0x10^{24}$	$0.6x10^{24}$	38.5	50
	-100		$8.1x10^{22}$		$8.0x10^{24}$	$0.6x10^{24}$	37.5	50
					$(8.0\pm0.0)x10^{24}$	$(0.6\pm0.0)x10^{24}$	37.9±0.4	50±0.0

4. Discussion

Consistent information about trapping sites density and trapping energies in three metallurgical states of PH13-8Mo was obtained using experimental data from permeation and TDS.

A maximum trapping energy E_T of about 53 kJ/mol has been found in H860 and H1000 states using TDS. On the other hand, a maximum binding energy E_B of about 49 kJ/mol has been found in these states from the simulation of permeation tests, which is consistent with TDS results. The E_T value of about 36 kJ/mol (peak 3) for H860 and H1000 states found by TDS is also in good agreement with the E_B value of 34 kJ/mol found by permeation simulation. The lowest trapping energy found using TDS (peak 2), of about 24 kJ/mol, cannot be studied with permeation, as this energy is too low to have any effect on permeation curves. This is because the trap occupancy of such traps is very low during our permeation tests according to the simulations (see *Fig.* 13 (a)). We remind that the hydrogen charging conditions used in this study are different for permeation specimens and TDS specimens. The lattice hydrogen concentration found in TDS (peak 1, *Fig.* 10. (c)) is about 10^{25} m^{-3} while it is only about 10^{23} m^{-3} at maximum at the entry side of permeation specimens considering equation (12), i.e. two orders of magnitude below pre-charged TDS samples. The occupancy of traps depends both on their binding energy and on the lattice hydrogen concentration. Consequently, the low energy traps may have a substantial effect on our TDS spectra (significant occupancy) while having almost no contribution to our permeation curves (very low occupancy).

A comment is also due here about the comparison of *trapping* energies (E_T in Fig. 1) obtained from TDS and the *binding* energies extracted from the simulation of permeation curves (E_B in Fig. 1). For intermediate and deep trapping in the H860 and H1000 states, the values of trapping (Table 6) and binding (Table 7) energies are almost equal ($E_T \approx E_B \approx$ 35 kJ/mol for intermediate trapping and $E_T \approx E_B \approx$ 50 kJ/mol for deep trapping). According to Eq. (1), this would suggest that the saddle point energy is very low, i.e. not higher than the uncertainty of the trapping and binding energies determined here (a few kJ/mol).

The microstructures of the three metallurgical states have been characterised to identify similarities and differences. These materials display the same grain size and dislocation density, however they differ by their precipitation state and austenite content, as summarised in *Fig. 4*. The trapping characteristics of the studied materials can be linked to these microstructural elements.

Dislocations have a well-known trapping effect on hydrogen [18], both in dislocation core (deep trapping) and dislocation strain field (reversible trapping, $\sim$ 30 kJ/mol), resulting in different trapping energies (see *Table.* 1). *Wei et al.* [15] studied hydrogen trapping in pure martensite (i.e. with no austenite and no precipitates). They found a mean trapping energy of 33.9 kJ/mol associated with dislocations, which is close from the binding energy of 37.9 kJ/mol that we found in the SA state of PH13-8Mo. They also found a trapping capacity of dislocations of 6.3-14.4 H atom/nm. Another study by *Mine et al*. [13] on pure martensite as well found that dislocations lines could trap 3.7 H atom/nm. We found a dislocation density of $5.1 \cdot 10^{14}\ m^{-2}$ in the SA state, which could then trap 2.1-8x10^{24} H atom/m^3 according to the results of these two studies. Using the Kumnick and Johnson analysis, we found a trap density of $8.6 \cdot 10^{24}\ m^{-3}$ in the SA state, which is then consistent with trapping by elastic field of dislocations. Therefore, dislocations could be the main microstructural feature responsible for hydrogen trapping in the non-aged state of PH13-8Mo.

Precipitates are also known to be effective trapping sites for hydrogen. The trapping of hydrogen on precipitates/matrix interface has been studied [24] and mainly relies on the creation of geometrically necessary dislocations (GND) accommodating semi-coherent or incoherent interfaces. However, considering the small size of the NiAl precipitates and their coherency with the matrix (interface misfit of only 0.7%), the creation of GNDs at precipitates/matrix interface is not expected here. Some hydrogen can also be trapped

in the elastic fields generated by precipitates [4,24,98,99]. The elastic fields are associated with low energy traps (see Table 1). According to previous works [21,98], the binding energy can be approximated as $\sigma_m \times V_H$, where $\sigma_m = K\varepsilon_m$, with σ_m and ε_m the hydrostatic stress and strain respectively, K the bulk modulus (160 GPa) and V_H the partial molar volume of hydrogen in the material (1.8 10^{-6} m^3/mol). The hydrostatic strain is maximum at the matrix-precipitate interface and is given by $\varepsilon_m = 2\delta/3$ [98], with δ is the lattice misfit. Considering 2.7% as an upper limit of δ, a maximum binding energy of 5 kJ/mol of hydrogen in the elastic fields of precipitates is obtained, which is significantly smaller than the energy corresponding to peak 2 of TDS. So we suppose that this peak does not correspond to trapping by elastic fields of precipitates.

Finally, hydrogen could be trapped in constitutional vacancies, which can form abundantly when the composition of an ordered phase (the B2-NiAl precipitates here) deviates from stoichiometry [100]. *Takahashi et al.* [27] studied the hydrogen trapping in constitutional vacancies of vanadium carbides in a precipitation-hardened ferritic steel, using TDS and atom probe tomography. It appears that hydrogen is not trapped in the bulk of the precipitates, because the saddle point energy is too high for hydrogen to enter the bulk constitutional vacancies. On the other hand, some hydrogen was trapped in constitutional vacancies close from the precipitate/matrix interface. The corresponding trapping energy was measured to be about 60 kJ/mol, which is slightly higher than the trapping energies reported for "conventional" vacancies in steel (see *Table.* 1). *Ma et al.* [26] studied hydrogen trapping in several coherent nano-precipitates, using DFT calculations. It was also concluded that hydrogen could be trapped in structural vacancies if those are located close from the precipitate/matrix interface. The authors found out that constitutional vacancies in B2-NiAl could be deep traps if they are located directly on the precipitate/matrix interface (E_B = 45-57 kJ/mol). In conclusion, the B2-NiAl precipitates in PH13-8Mo are not supposed to contribute strongly to the hydrogen trapping, especially concerning the intermediate trapping. Nevertheless, it cannot be excluded that the constitutional vacancies of these precipitates have a contribution to the deep trapping observed. Such contribution, however, is hard to quantify in the scope of this study because only a slight increase of hydrogen content associated with peak 4 was observed with the addition of precipitates.

The austenitic phase can also contribute to hydrogen trapping, either as bulk trapping or by trapping at the austenite/martensite interface. When comparing the austenite contents in the three metallurgical states (see *Fig. 4* and Table 3) and the corresponding trap densities measured using permeation tests and simulation (see Table 4 and Table 7), it appears that the increase in trap density is mainly correlated to the increase in austenite volume between the SA and H860 states, while it is not between the H860 and H1000 states. Thus, the volume of austenite is not the only parameter influencing hydrogen trapping. Therefore, the effect of hydrogen trapping at the austenite/martensite interface should be considered. *Fielding et al.* [35] studied the effect of austenite content on hydrogen penetration in bainitic steels containing various amounts of austenite, with either a lath-like morphology or a blocky morphology. The authors deducted that the austenite morphology has a very strong effect on the penetration of hydrogen into the steel, the lath-like morphology causing a far more important decrease in hydrogen apparent diffusivity than the blocky morphology. Our analyses suggest that the *retained* austenite in PH13-8Mo mainly consists of inter-lath and intra-lath islands. On the other hand, we observed *reverted* austenite mainly as thin inter-lath layers. These layers were about 10 nm thick in the H1000 state. A simple calculation, shown earlier, considering the austenite volume fraction, martensitic lath size, and austenite layer thickness, suggested that reverted austenite forms homogeneously on all lath boundaries during ageing. In the SA state, the material contains a small volume fraction of retained austenite. Moreover, the retained austenite displays a small surface to volume ratio due to its island morphology. Therefore, the austenitic phase in the SA state has a low hydrogen trapping effect, both in the bulk and at the austenite/martensite interface. Ageing the material in the H860 condition led to a small increase in austenite content, but to a strong increase in trap density. The reverted

austenite that formed in the H860 state has a high surface to volume ratio due to its layer morphology, resulting in a high trapping capacity at the austenite/martensite interface despite the overall limited volume of reverted austenite. The increase in austenite content between the H860 and H1000 states is similar to the one between the SA and H860 states. However, in the H1000 state the trap density measured in permeation is not significantly higher than the one measured in the H860 state. Supposing that the reverted austenite forms homogeneously on all lath boundaries, as suggested before, it can be considered that very thin layers of reverted austenite are already formed on all lath boundaries in the H860 state. Then, the increase in reverted austenite content in the H1000 state would be the result of the thickening of these layers, and not the result of the formation of new layers. Therefore, the increase in austenite volume between the H860 and H1000 states would result in a negligible change in the total austenite/martensite interface area, accounting for the almost unchanged trap density measured using permeation. A similar trend was reported by *Fielding et al.*, who observed that once the austenite layers are developed enough to percolate with each other a further increase in the austenite content had little effect on hydrogen apparent diffusivity in the material.

We previously estimated a lath boundary density of $2.5 \cdot 10^6\ m^{-1}$. Considering reverted austenite presence on all lath boundaries would then lead to an austenite/martensite interface density of $5 \cdot 10^6\ m^{-1}$. If we consider a trapping ability of one hydrogen atom per Burgers vector squared in the austenite/martensite interface [12], the austenite/martensite interface in the aged materials would correspond to a trap density of $6.1 \cdot 10^{25}\ m^{-3}$. From the Kumnick and Johnsons analyses, the increase in trap density compared to the SA state (which contains no reverted austenite) is of $4.7 \cdot 10^{25}\ m^{-3}$ for the H860 state and $5.6 \cdot 10^{25}\ m^{-3}$ for the H1000 state (see Table.4). This is in good agreement with the previous value estimated from microstructural considerations. Consequently, we consider that the austenite/martensite interfaces are the main hydrogen trapping site responsible for the modification of permeation curves between the SA state and the aged states. These interfaces would correspond to a majority of intermediate traps and a minority of deep traps. The intermediate energy (E_B = 35 kJ/mol) and deep trapping energy (E_B = 50 kJ/mol) are in the range of energies obtained by other authors for the trapping on grain boundaries [12,72,76]. The interpretation that intermediate trapping is related to austenite/martensite interfaces is also consistent with the dependence on ageing treatment of peak 3 of TDS (*Fig.* 10 (c)) showing a strong variation of the hydrogen concentration in intermediate traps between SA and H860 states and a more limited variation between H860 and H1000 states.

Eventually, even if bulk trapping in the austenitic phase does not seem to be relevant in the materials studied here, one must consider that the corresponding trapping/binding energy might simply be too low for us to quantify such traps using permeation tests, as explained before. Indeed, studies suggest that austenite bulk trapping is associated with binding energies in the range 10 to 20 kJ/mol with respect to the martensitic/ferritic matrix [76,101]. Hence, the observed intensification of peak 2 of TDS with rising ageing temperature (see *Fig.* 10 (c)) might be associated with bulk trapping in retained/reverted austenite. On the other hand, *Turk et al.* [102] performed a detailed study of hydrogen bulk trapping in austenite, and concluded that it cannot be rightly described as point traps under the assumption of local equilibrium. However, the size of the austenite islands in their study was in the micrometre range. In contrast here, the thickness of austenite layers is of the order of 10 nm only. Considering a diffusion coefficient of about 10^{-15} m²/s [103] in austenite, the time needed for hydrogen to travel 10 nm is as short as 0.1 s, which is orders of magnitude shorter than the permeation times measured in this study (or than the charging times used before TDS). Thus it seems reasonable in our case to assume that austenite is equilibrated with the surrounding martensite at any time.

5. Conclusions

In this study, the hydrogen trapping behaviour of a PH13-8Mo maraging stainless steel was investigated using electrochemical permeation and TDS, as well as numerical simulation of permeation. Different metallurgical states of the material were studied, and their microstructural similarities and differences were clearly identified. Eventually, the hydrogen trap densities and trap energies were quantified and associated with specific microstructural features. Using this unique combination of experimental and modelling approaches, and a significant amount of experimental data, new results and/or confirmation of assumptions proposed in literature could be obtained:

- The solution annealed material contains no B2-NiAl precipitates nor reverted austenite. Its martensitic structure contains a high dislocation density, and a majority of low angle boundaries, such as lath boundaries, which behave as dislocation walls. In this state, the identified trap population mainly consists of intermediate energy traps (~35 kJ/mol). The trap density and the trap energy are in good accordance with trapping by dislocations. A little amount of retained austenite was identified but had no significant impact on trapping.

- The ageing of the material, leading to formation of B2-NiAl precipitates and reverted austenite, caused a strong increase in trap density, while the dislocation density was not affected. Permeation showed the existence of a majority of intermediate energy traps (~35 kJ/mol), with a minority of deep energy traps (~50 kJ/mol). Further ageing of the material led to an increase in reverted austenite content, that had limited effect on intermediate and deep trapping.

- The analysis of B2-NiAl precipitates led us to conclude that their trapping capabilities are very low, as suggested by other studies. Thus, the increase in trap density consecutive to ageing is not believed to be caused by this microstructural feature. However, it cannot be excluded that the constitutional vacancies of B2-NiAl located close to the precipitate/matrix interface have some contribution to the deep trapping of hydrogen (~50 kJ/mol).

- The analysis of reverted austenite revealed that this phase is very finely spread inside the material microstructure. This results in a high density of austenite/martensite interfaces which is well correlated with the increase in trap density observed after ageing. The observed intermediate and deep trapping energies are consistent with trapping by grain boundaries, which makes sense in the case of trapping by austenite/martensite interface. Moreover, the morphology of reverted austenite, present as inter-lath layers, implies that an increase in the phase volume will result in a negligible increase in interphase boundary area. We observed no significant difference in intermediate and deep trap density between the two aged states of the material, which yet contain different amount of reverted austenite. Thus, we concluded that intermediate trapping (~35 kJ/mol) and deep trapping (~50 kJ/mol) mainly occurs on the austenite/martensite interfaces, and not in the bulk of reverted austenite.

- While permeation and TDS results are in good agreement, the analysis of TDS data revealed an additional trap population, associated with a shallow energy. We were not able to quantify these traps using permeation, as they have a very low influence on permeation curves because of their low binding energy. Estimation of the hydrogen concentration in these traps using TDS reveals that

it increases between the two aged states. This observation, as well as the measured trap energy (~20 kJ/mol), seems consistent with trapping in the bulk of reverted austenite.

6. Declaration of competing interest

The authors declare that they have no known competing financial interests or personal relationships that could have appeared to influence the work reported in this paper.

7. Acknowledgements

This research was mainly funded by Aubert & Duval and Airbus, with the support of ANRT (Association Nationale de la Recherche et de la Technologie).

Fruitful discussions in the CASHMERE R&T consortium (Airbus, Aubert & Duval, University of Manchester, Mines Saint-Etienne, La Rochelle University and French Corrosion Institute) are acknowledged, as well as the material supplied by Aubert & Duval.

The authors wish to express their sincere thanks to Cyril Berziou, Rémi Milet, Nathalie Peillon, Marilyne Mondon, Max Boudes, Gilles Blanc and Yiyang Wang. They also acknowledge the Consortium Lyon Saint-Etienne de Microscopie (CLYM, FED 4092) for the access to the Jeol JEM-ARM200F NEO-ARM microscope, as well as Saint-Étienne Metropole for financial support in the frame of CPER 2015-2020.

8. Appendix

The Fe-12Cr model alloy was produced in the laboratory, with a very low impurity content as shown in *Table.* 1. The material was produced in the as-forged state, with a high dislocation density. In order to reduce the amount of hydrogen traps due to lattice defects, the material was then annealed at 850°C during 4h followed by slow cooling inside the furnace. The annealed material has a lower dislocation density and a larger grain size, which was measured to be 350 µm using chemical etching (Vilella's reagent) and optical microscopy. As shown in Fig. 16, the annealed material shows a coarse grain ferritic microstructure.

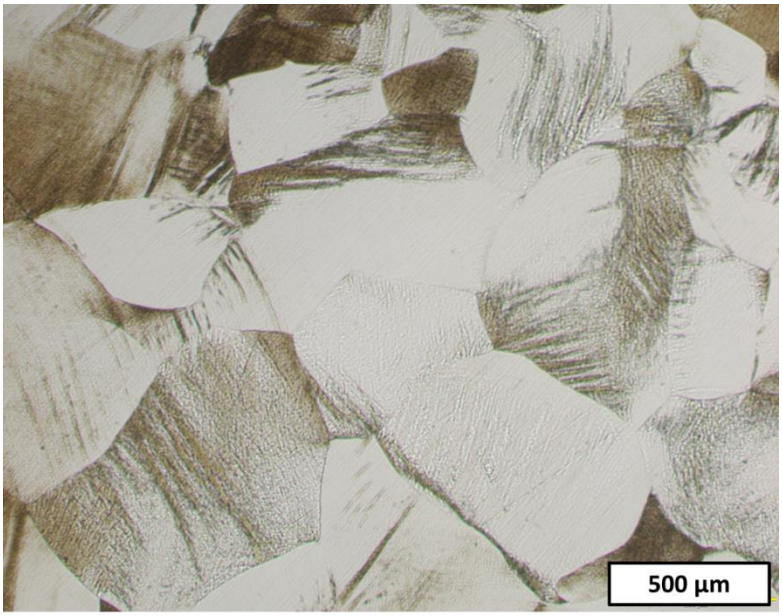

Fig. 16. Optical micrograph of Fe-12Cr in the annealed state after etching.

Permeation tests were performed on this Fe-12Cr model alloy in order to measure the hydrogen diffusivity in a very pure BCC alloy with a chromium content close to that of PH13-8Mo. Because of the higher hydrogen diffusivity in such material compared to PH13-8Mo, thicker samples were used (1.5 mm). A charging current density of -1000 µA/cm^2 was used until the permeation current reached a steady state. The rising permeation transients of the as-forged and annealed states are presented in *Fig.* 17. It can be seen that the hydrogen exit time is much shorter for the annealed sample compared to the as-forged sample, thus confirming the effect of annealing on hydrogen trapping. The hydrogen apparent diffusivity in the two material states were measured using:

$$D_{app} = \frac{e^2}{25 \cdot t_{1\%}} \quad (15)$$

Where e is the sample thickness (1.5 mm) and $t_{1\%}$ is the duration required to reach 1% of the steady state current density. The values of $t_{1\%}$ and D_{app} are given in *Table.* 8. A hydrogen apparent diffusivity of about 10^{-10} m^2/s was found in the annealed material. Considering that the annealed state of the Fe-12Cr model alloy has both a very low amount of lattice defects and a chromium content similar to that of PH13-8Mo, this value of apparent diffusivity is considered to be very close to the lattice diffusivity in the martensitic phase of PH13-8Mo. Thus, a hydrogen lattice diffusivity value of 10^{-10} m^2/s was used in this study to model hydrogen diffusion and trapping in PH13-8Mo.

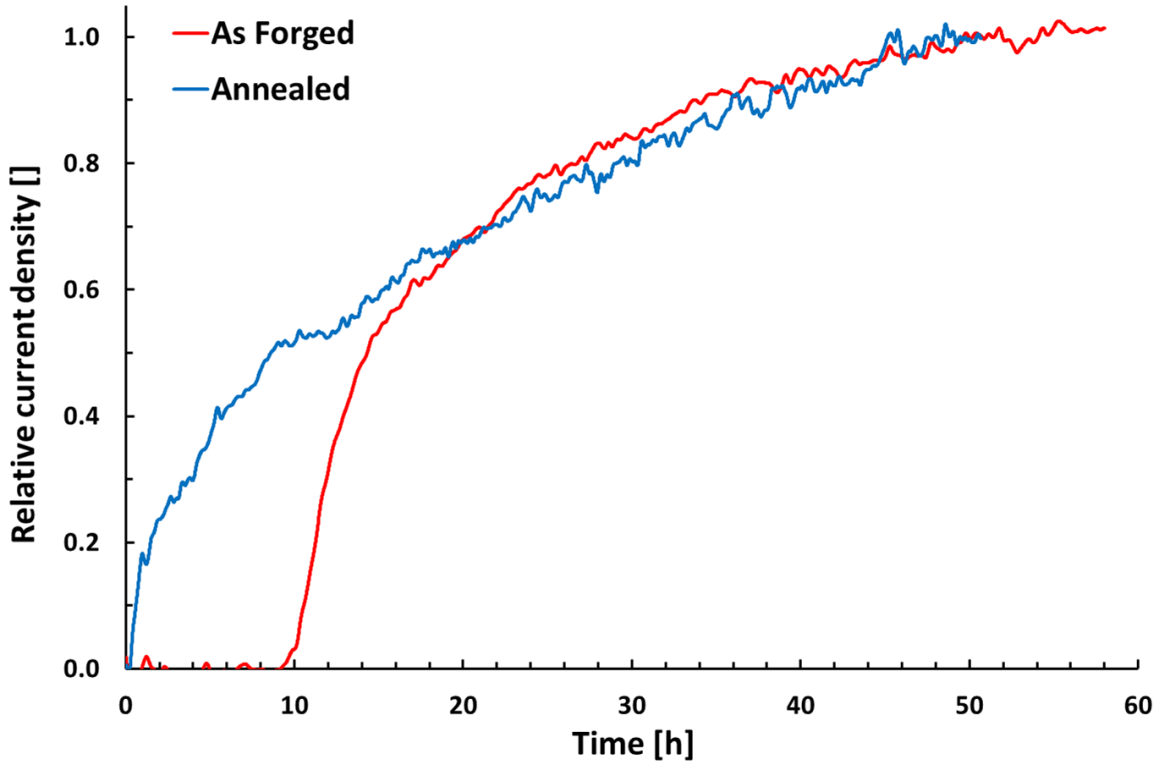

Fig. 17. Permeation rising transients of the Fe-12Cr model alloy in the as-forged state and after annealing (charging current density -1000 µA/cm2).

Table. 8. Values of $t_{1\%}$ and D_{app} measured in the two states of Fe-12Cr model alloy from the permeation rising transients.

State	$t_{1\%}$ [s]	D_{app} [m^2/s]
As Forged	34300	2.6×10^{-12}
Annealed	930	9.7×10^{-11}

9. Data availability statement

The raw and processed data required to reproduce these findings are available from the corresponding author upon request.

10. References

[1] W.H. Johnson, On Some Remarkable Changes Produced in Iron and Steel by the Action of Hydrogen and Acids, Nature. 11 (1875) 393–393. https://doi.org/10.1038/011393a0.

[2] R. Gangloff, Hydrogen Assisted Cracking of High Strength Alloys, (2003) 195.

[3] J. Song, W.A. Curtin, Atomic mechanism and prediction of hydrogen embrittlement in iron, Nature Mater. 12 (2013) 145–151. https://doi.org/10.1038/nmat3479.

[4] C. Rousseau, A. Oudriss, R. Milet, X. Feaugas, M. El May, N. Saintier, Q. Tonizzo, M. Msakni-Malouche, Effect of aging treatment on apparent hydrogen solubility and trapping in a new generation maraging steel, Scripta Materialia. 183 (2020) 144–148. https://doi.org/10.1016/j.scriptamat.2020.03.013.

[5] J. Bestautte, S. Kalácska, D. Béchet, Z. Obadia, F. Christien, Investigation of quasi-cleavage in a hydrogen charged maraging stainless steel, Corrosion Science. 218 (2023) 111163. https://doi.org/10.1016/j.corsci.2023.111163.

[6] F. Martin, X. Feaugas, A. Oudriss, D. Tanguy, L. Briottet, J. Kittel, 8 - State of Hydrogen in Matter: Fundamental Ad/Absorption, Trapping and Transport Mechanisms, in: C. Blanc, I. Aubert (Eds.), Mechanics - Microstructure - Corrosion Coupling, Elsevier, 2019: pp. 171–197. https://doi.org/10.1016/B978-1-78548-309-7.50008-9.

[7] A. Oudriss, F. Martin, X. Feaugas, 11 - Experimental Techniques for Dosage and Detection of Hydrogen, in: C. Blanc, I. Aubert (Eds.), Mechanics - Microstructure - Corrosion Coupling, Elsevier, 2019: pp. 245–268. https://doi.org/10.1016/B978-1-78548-309-7.50011-9.

[8] X. Liu, W. Xie, W. Chen, H. Zhang, Effects of grain boundary and boundary inclination on hydrogen diffusion in α-iron, J. Mater. Res. 26 (2011) 2735–2743. https://doi.org/10.1557/jmr.2011.262.

[9] A. Oudriss, J. Creus, J. Bouhattate, E. Conforto, C. Berziou, C. Savall, X. Feaugas, Grain size and grain-boundary effects on diffusion and trapping of hydrogen in pure nickel, Acta Materialia. 60 (2012) 6814–6828. https://doi.org/10.1016/j.actamat.2012.09.004.

[10] K.N. Solanki, M.A. Tschopp, M.A. Bhatia, N.R. Rhodes, Atomistic Investigation of the Role of Grain Boundary Structure on Hydrogen Segregation and Embrittlement in α-Fe, Metall and Mat Trans A. 44 (2013) 1365–1375. https://doi.org/10.1007/s11661-012-1430-z.

[11] E.I. Galindo-Nava, P.E.J. Rivera-Díaz-del-Castillo, A model for the microstructure behaviour and strength evolution in lath martensite, Acta Materialia. 98 (2015) 81–93. https://doi.org/10.1016/j.actamat.2015.07.018.

[12] A. Turk, G.R. Joshi, M. Gintalas, M. Callisti, P.E.J. Rivera-Díaz-del-Castillo, E.I. Galindo-Nava, Quantification of hydrogen trapping in multiphase steels: Part I – Point traps in martensite, Acta Materialia. 194 (2020) 118–133. https://doi.org/10.1016/j.actamat.2020.05.007.

[13] Y. Mine, Z. Horita, Y. Murakami, Effect of high-pressure torsion on hydrogen trapping in Fe–0.01mass% C and type 310S austenitic stainless steel, Acta Materialia. 58 (2010) 649–657. https://doi.org/10.1016/j.actamat.2009.09.043.

[14] Y. Momotani, A. Shibata, T. Yonemura, Y. Bai, N. Tsuji, Effect of initial dislocation density on hydrogen accumulation behavior in martensitic steel, Scripta Materialia. 178 (2020) 318–323. https://doi.org/10.1016/j.scriptamat.2019.11.051.

[15] F.-G. Wei, K. Tsuzaki, Response of hydrogen trapping capability to microstructural change in tempered Fe–0.2C martensite, Scripta Materialia. 52 (2005) 467–472. https://doi.org/10.1016/j.scriptamat.2004.11.008.

[16] R. Matsumoto, S. Taketomi, N. Miyazaki, Y. Inoue, Estimation of hydrogen distribution around dislocations based on first principles calculations, (n.d.) 8.
[17] S. Taketomi, R. Matsumoto, N. Miyazaki, Atomistic study of hydrogen distribution and diffusion around a {112} edge dislocation in alpha iron, Acta Materialia. 56 (2008) 3761–3769. https://doi.org/10.1016/j.actamat.2008.04.011.
[18] S. Frappart, A. Oudriss, X. Feaugas, J. Creus, J. Bouhattate, F. Thébault, L. Delattre, H. Marchebois, Hydrogen trapping in martensitic steel investigated using electrochemical permeation and thermal desorption spectroscopy, Scripta Materialia. 65 (2011) 859–862. https://doi.org/10.1016/j.scriptamat.2011.07.042.
[19] S. Ifergane, E. Sabatani, B. Carmeli, Z. Barkay, V. Ezersky, O. Beeri, N. Eliaz, Hydrogen diffusivity measurement and microstructural characterization of Custom 465 stainless steel, Electrochimica Acta. 178 (2015) 494–503. https://doi.org/10.1016/j.electacta.2015.08.016.
[20] M. Shmulevitsh, S. Ifergane, M. Eliaz, R.Z. Shneck, Diffusion and trapping of hydrogen due to elastic interaction with η-Ni3Ti precipitates in Custom 465® stainless steel, International Journal of Hydrogen Energy. 44 (2019) 31610–31620. https://doi.org/10.1016/j.ijhydene.2019.09.197.
[21] L. Cupertino-Malheiros, A. Oudriss, F. Thébault, M. Piette, X. Feaugas, Hydrogen Diffusion and Trapping in Low-Alloy Tempered Martensitic Steels, Metall Mater Trans A. 54 (2023) 1159–1173. https://doi.org/10.1007/s11661-023-06967-4.
[22] P. Schutz, F. Martin, Q. Auzoux, J. Adem, E.F. Rauch, Y. Wouters, L. Latu-Romain, Hydrogen transport in 17−4 PH stainless steel: Influence of the metallurgical state on hydrogen diffusion and trapping, Materials Characterization. 192 (2022) 112239. https://doi.org/10.1016/j.matchar.2022.112239.
[23] L.B. Peral, Z. Amghouz, C. Colombo, I. Fernández-Pariente, Evaluation of hydrogen trapping and diffusion in two cold worked CrMo(V) steel grades by means of the electrochemical hydrogen permeation technique, Theoretical and Applied Fracture Mechanics. 110 (2020) 102771. https://doi.org/10.1016/j.tafmec.2020.102771.
[24] F.G. Wei, K. Tsuzaki, Quantitative analysis on hydrogen trapping of TiC particles in steel, Metall and Mat Trans A. 37 (2006) 331–353. https://doi.org/10.1007/s11661-006-0004-3.
[25] X. Li, J. Zhang, Q. Fu, E. Akiyama, X. Song, S. Shen, Q. Li, Hydrogen embrittlement of high strength steam turbine last stage blade steels: Comparison between PH17-4 steel and PH13-8Mo steel, Materials Science and Engineering: A. 742 (2019) 353–363. https://doi.org/10.1016/j.msea.2018.10.086.
[26] Y. Ma, Y. Shi, H. Wang, Z. Mi, Z. Liu, L. Gao, Y. Yan, Y. Su, L. Qiao, A first-principles study on the hydrogen trap characteristics of coherent nano-precipitates in α-Fe, International Journal of Hydrogen Energy. 45 (2020) 27941–27949. https://doi.org/10.1016/j.ijhydene.2020.07.123.
[27] J. Takahashi, Origin of hydrogen trapping site in vanadium carbide precipitation strengthening steel, Acta Materialia. (2018) 12.
[28] P.W. Hochanadel, G.R. Edwards, C.V. Robino, M.J. Cieslak, Heat treatment of investment cast PH 13-8 Mo stainless steel: Part I. Mechanical properties and microstructure, Metallurgical and Materials Transactions A. 25 (1994) 789–798. https://doi.org/10.1007/BF02665455.
[29] D.H. Ping, M. Ohnuma, Y. Hirakawa, Y. Kadoya, K. Hono, Microstructural evolution in 13Cr–8Ni–2.5Mo–2Al martensitic precipitation-hardened stainless steel, Materials

Science and Engineering: A. 394 (2005) 285–295. https://doi.org/10.1016/j.msea.2004.12.002.
[30] V. Seetharaman, M. Sundararaman, R. Krishnan, Precipitation hardening in a PH 13-8 Mo stainless steel, Materials Science and Engineering. 47 (1981) 1–11. https://doi.org/10.1016/0025-5416(81)90034-3.
[31] H.K.D.H. Bhadeshia, Prevention of Hydrogen Embrittlement in Steels, ISIJ International. 56 (2016) 24–36. https://doi.org/10.2355/isijinternational.ISIJINT-2015-430.
[32] V. Olden, A. Saai, L. Jemblie, R. Johnsen, FE simulation of hydrogen diffusion in duplex stainless steel, International Journal of Hydrogen Energy. 39 (2014) 1156–1163. https://doi.org/10.1016/j.ijhydene.2013.10.101.
[33] L. Couturier, F. De Geuser, M. Descoins, A. Deschamps, Evolution of the microstructure of a 15-5PH martensitic stainless steel during precipitation hardening heat treatment, Materials & Design. 107 (2016) 416–425. https://doi.org/10.1016/j.matdes.2016.06.068.
[34] R. Schnitzer, R. Radis, M. Nöhrer, M. Schober, R. Hochfellner, S. Zinner, E. Povoden-Karadeniz, E. Kozeschnik, H. Leitner, Reverted austenite in PH 13-8 Mo maraging steels, Materials Chemistry and Physics. 122 (2010) 138–145. https://doi.org/10.1016/j.matchemphys.2010.02.058.
[35] L.C.D. Fielding, E.J. Song, D.K. Han, H.K.D.H. Bhadeshia, D.-W. Suh, Hydrogen diffusion and the percolation of austenite in nanostructured bainitic steel, Proc. R. Soc. A. 470 (2014) 20140108. https://doi.org/10.1098/rspa.2014.0108.
[36] Y.H. Fan, B. Zhang, H.L. Yi, G.S. Hao, Y.Y. Sun, J.Q. Wang, E.-H. Han, W. Ke, The role of reversed austenite in hydrogen embrittlement fracture of S41500 martensitic stainless steel, Acta Materialia. 139 (2017) 188–195. https://doi.org/10.1016/j.actamat.2017.08.011.
[37] S.L.I. Chan, H.L. Lee, J.R. Yang, Effect of retained austenite on the hydrogen content and effective diffusivity of martensitic structure, MTA. 22 (1991) 2579–2586. https://doi.org/10.1007/BF02851351.
[38] B.A. Szost, R.H. Vegter, P.E.J. Rivera-Díaz-del-Castillo, Hydrogen-Trapping Mechanisms in Nanostructured Steels, Metall and Mat Trans A. 44 (2013) 4542–4550. https://doi.org/10.1007/s11661-013-1795-7.
[39] A. Turnbull, Hydrogen diffusion and trapping in metals, in: Gaseous Hydrogen Embrittlement of Materials in Energy Technologies, Elsevier, 2012: pp. 89–128. https://doi.org/10.1533/9780857095374.1.89.
[40] A. Turnbull, R.B. Hutchings, Analysis of hydrogen atom transport in a two-phase alloy, Materials Science and Engineering: A. 177 (1994) 161–171. https://doi.org/10.1016/0921-5093(94)90488-X.
[41] W.Y. Choo, J.Y. Lee, Thermal analysis of trapped hydrogen in pure iron, MTA. 13 (1982) 135–140. https://doi.org/10.1007/BF02642424.
[42] H.E. Kissinger, Variation of peak temperature with heating rate in differential thermal analysis, J. RES. NATL. BUR. STAN. 57 (1956) 217. https://doi.org/10.6028/jres.057.026.
[43] A. Drexler, L. Vandewalle, T. Depover, K. Verbeken, J. Domitner, Critical verification of the Kissinger theory to evaluate thermal desorption spectra, International Journal of Hydrogen Energy. 46 (2021) 39590–39606. https://doi.org/10.1016/j.ijhydene.2021.09.171.
[44] L. Claeys, V. Cnockaert, T. Depover, I. De Graeve, K. Verbeken, Critical assessment of the evaluation of thermal desorption spectroscopy data for duplex stainless steels: A

combined experimental and numerical approach, Acta Materialia. 186 (2020) 190–198. https://doi.org/10.1016/j.actamat.2019.12.055.
[45] E. Legrand, A. Oudriss, C. Savall, J. Bouhattate, X. Feaugas, Towards a better understanding of hydrogen measurements obtained by thermal desorption spectroscopy using FEM modeling, International Journal of Hydrogen Energy. 40 (2015) 2871–2881. https://doi.org/10.1016/j.ijhydene.2014.12.069.
[46] Q. Liu, A.D. Atrens, Z. Shi, K. Verbeken, A. Atrens, Determination of the hydrogen fugacity during electrolytic charging of steel, Corrosion Science. 87 (2014) 239–258. https://doi.org/10.1016/j.corsci.2014.06.033.
[47] E. Legrand, J. Bouhattate, X. Feaugas, H. Garmestani, Computational analysis of geometrical factors affecting experimental data extracted from hydrogen permeation tests: II – Consequences of trapping and an oxide layer, International Journal of Hydrogen Energy. 37 (2012) 13574–13582. https://doi.org/10.1016/j.ijhydene.2012.06.043.
[48] A.J. Kumnick, H.H. Johnson, Deep trapping states for hydrogen in deformed iron, Acta Metallurgica. 28 (1980) 33–39. https://doi.org/10.1016/0001-6160(80)90038-3.
[49] F. Montupet-Leblond, L. Corso, M. Payet, R. Delaporte-Mathurin, E. Bernard, Y. Charles, J. Mougenot, S. Vartanian, E.A. Hodille, C. Grisolia, Permeation and trapping of hydrogen in Eurofer97, Nuclear Materials and Energy. 29 (2021) 101062. https://doi.org/10.1016/j.nme.2021.101062.
[50] A. Díaz, A. Zafra, E. Martínez-Pañeda, J.M. Alegre, J. Belzunce, I.I. Cuesta, Simulation of hydrogen permeation through pure iron for trapping and surface phenomena characterisation, Theoretical and Applied Fracture Mechanics. 110 (2020) 102818. https://doi.org/10.1016/j.tafmec.2020.102818.
[51] A. Drexler, W. Siegl, W. Ecker, M. Tkadletz, G. Klösch, H. Schnideritsch, G. Mori, J. Svoboda, F.D. Fischer, Cycled hydrogen permeation through Armco iron – A joint experimental and modeling approach, Corrosion Science. 176 (2020) 109017. https://doi.org/10.1016/j.corsci.2020.109017.
[52] R. Kirchheim, Changing the interfacial composition of carbide precipitates in metals and its effect on hydrogen trapping, Scripta Materialia. 160 (2019) 62–65. https://doi.org/10.1016/j.scriptamat.2018.09.043.
[53] E.A. Hodille, Modelling of hydrogen isotopes trapping, diffusion and permeation in divertor monoblocks under ITER-like conditions, Nuclear Fusion. 61 (2021). https://doi.org/10.1088/1741-4326/ac2abc.
[54] C. Hurley, F. Martin, L. Marchetti, J. Chêne, C. Blanc, E. Andrieu, Numerical modeling of thermal desorption mass spectroscopy (TDS) for the study of hydrogen diffusion and trapping interactions in metals, International Journal of Hydrogen Energy. 40 (2015) 3402–3414. https://doi.org/10.1016/j.ijhydene.2015.01.001.
[55] J.B. Leblond, D. Dubois, A general mathematical description of hydrogen diffusion in steels—II. Numerical study of permeation and determination of trapping parameters, Acta Metallurgica. 31 (1983) 1471–1478. https://doi.org/10.1016/0001-6160(83)90143-8.
[56] A. McNabb, P.K. Foster, A new analysis of the diffusion of hydrogen in iron and ferritic steels, Journal of Transaction of the Metallurgical Society of AIME. 227 (1963) 618–627.
[57] J. Bouhattate, E. Legrand, X. Feaugas, Computational analysis of geometrical factors affecting experimental data extracted from hydrogen permeation tests: I – Consequences of trapping, International Journal of Hydrogen Energy. 36 (2011) 12644–12652. https://doi.org/10.1016/j.ijhydene.2011.06.143.

[58] A. Drexler, T. Depover, S. Leitner, K. Verbeken, W. Ecker, Microstructural based hydrogen diffusion and trapping models applied to Fe–C X alloys, Journal of Alloys and Compounds. 826 (2020) 154057. https://doi.org/10.1016/j.jallcom.2020.154057.
[59] R. Kirchheim, Bulk Diffusion-Controlled Thermal Desorption Spectroscopy with Examples for Hydrogen in Iron, Metall and Mat Trans A. 47 (2016) 672–696. https://doi.org/10.1007/s11661-015-3236-2.
[60] R. A. Oriani, The diffusion and trapping of hydrogen in steel, Acta Metallurgica. 18 (1970).
[61] E.J. Song, D.-W. Suh, H.K.D.H. Bhadeshia, Theory for hydrogen desorption in ferritic steel, Computational Materials Science. 79 (2013) 36–44. https://doi.org/10.1016/j.commatsci.2013.06.008.
[62] J. Svoboda, F.D. Fischer, Modelling for hydrogen diffusion in metals with traps revisited, Acta Materialia. 60 (2012) 1211–1220. https://doi.org/10.1016/j.actamat.2011.11.025.
[63] A. Turk, D. San Martín, P.E.J. Rivera-Díaz-del-Castillo, E.I. Galindo-Nava, Correlation between vanadium carbide size and hydrogen trapping in ferritic steel, Scripta Materialia. 152 (2018) 112–116. https://doi.org/10.1016/j.scriptamat.2018.04.013.
[64] J. Toribio, V. Kharin, A generalised model of hydrogen diffusion in metals with multiple trap types, Philosophical Magazine. 95 (2015) 3429–3451. https://doi.org/10.1080/14786435.2015.1079660.
[65] E. Legrand, A. Oudriss, S. Frappart, J. Creus, X. Feaugas, J. Bouhattate, Computational analysis of geometrical factors affecting experimental data extracted from hydrogen permeation tests: III – Comparison with experimental results from the literature, International Journal of Hydrogen Energy. 39 (2014) 1145–1155. https://doi.org/10.1016/j.ijhydene.2013.10.099.
[66] D. Di Stefano, R. Nazarov, T. Hickel, J. Neugebauer, M. Mrovec, C. Elsässer, First-principles investigation of hydrogen interaction with TiC precipitates in $\ensuremath{\alpha}$-Fe, Phys. Rev. B. 93 (2016) 184108. https://doi.org/10.1103/PhysRevB.93.184108.
[67] D.E. Jiang, E.A. Carter, Diffusion of interstitial hydrogen into and through bcc Fe from first principles, Phys. Rev. B. 70 (2004) 064102. https://doi.org/10.1103/PhysRevB.70.064102.
[68] R.L.S. Thomas, D. Li, R.P. Gangloff, J.R. Scully, Trap-governed hydrogen diffusivity and uptake capacity in ultrahigh-strength AERMET 100 steel, Metall and Mat Trans A. 33 (2002) 1991–2004. https://doi.org/10.1007/s11661-002-0032-6.
[69] E. Van den Eeckhout, A. Laureys, Y. Van Ingelgem, K. Verbeken, Hydrogen permeation through deformed and heat-treated Armco pure iron, Materials Science and Technology. 33 (2017) 1515–1523. https://doi.org/10.1080/02670836.2017.1342015.
[70] S. Ifergane, R.B. David, E. Sabatani, B. Carmeli, O. Beeri, N. Eliaz, Hydrogen Diffusivity and Trapping in Custom 465 Stainless Steel, J. Electrochem. Soc. 165 (2018) C107–C115. https://doi.org/10.1149/2.0261803jes.
[71] K. Ono, M. Meshii, Hydrogen detrapping from grain boundaries and dislocations in high purity iron, Acta Metallurgica et Materialia. 40 (1992) 1357–1364. https://doi.org/10.1016/0956-7151(92)90436-I.
[72] R. Matsumoto, M. Riku, S. Taketomi, N. Miyazaki, Hydrogen–Grain Boundary Interaction in Fe, Fe–C, and Fe–N Systems, Progress in Nuclear Science and Technology. 2 (2011) 9–15. https://doi.org/10.15669/pnst.2.9.
[73] M. Yamaguchi, K.-I. Ebihara, M. Itakura, T. Kadoyoshi, T. Suzudo, H. Kaburaki, First-Principles Study on the Grain Boundary Embrittlement of Metals by Solute Segregation:

Part II. Metal (Fe, Al, Cu)-Hydrogen (H) Systems, Metall and Mat Trans A. 42 (2011) 330–339. https://doi.org/10.1007/s11661-010-0380-6.
[74] A.S. Kholtobina, R. Pippan, L. Romaner, D. Scheiber, W. Ecker, V.I. Razumovskiy, Hydrogen Trapping in bcc Iron, Materials. 13 (2020) 2288. https://doi.org/10.3390/ma13102288.
[75] W.A. Counts, C. Wolverton, R. Gibala, First-principles energetics of hydrogen traps in α-Fe: Point defects, Acta Materialia. 58 (2010) 4730–4741. https://doi.org/10.1016/j.actamat.2010.05.010.
[76] T. Hickel, R. Nazarov, E.J. McEniry, G. Leyson, B. Grabowski, J. Neugebauer, Ab Initio Based Understanding of the Segregation and Diffusion Mechanisms of Hydrogen in Steels, JOM. 66 (2014) 1399–1405. https://doi.org/10.1007/s11837-014-1055-3.
[77] D. Li, R.P. Gangloff, J.R. Scully, Hydrogen trap states in ultrahigh-strength AERMET 100 steel, Metall and Mat Trans A. 35 (2004) 849–864. https://doi.org/10.1007/s11661-004-0011-1.
[78] A. Taha, P. Sofronis, A micromechanics approach to the study of hydrogen transport and embrittlement, Engineering Fracture Mechanics. 68 (2001) 803–837. https://doi.org/10.1016/S0013-7944(00)00126-0.
[79] L. Li, B. Song, J. Cheng, Z. Yang, Z. Cai, Effects of vanadium precipitates on hydrogen trapping efficiency and hydrogen induced cracking resistance in X80 pipeline steel, International Journal of Hydrogen Energy. 43 (2018) 17353–17363. https://doi.org/10.1016/j.ijhydene.2018.07.110.
[80] X. Mei, Y. Yan, L. Qiao, Research on hydrogen embrittlement behavior of L-PBF 18Ni(300) maraging steel by experiments and numerical simulations, Acta Materialia. 256 (2023) 119141. https://doi.org/10.1016/j.actamat.2023.119141.
[81] T. Nyyssönen, M. Isakov, P. Peura, V.-T. Kuokkala, Iterative Determination of the Orientation Relationship Between Austenite and Martensite from a Large Amount of Grain Pair Misorientations, Metall and Mat Trans A. 47 (2016) 2587–2590. https://doi.org/10.1007/s11661-016-3462-2.
[82] G.K. Williamson, W.H. Hall, X-ray line broadening from filed aluminium and wolfram, Acta Metallurgica. 1 (1953) 22–31. https://doi.org/10.1016/0001-6160(53)90006-6.
[83] R. McKibben, R.M. Sharp, D.A. Harrington, B.G. Pound, G.A. Wright, A potentiostatic double-step method for measuring hydrogen atom diffusion and trapping in metal electrodes—I. Theory, Acta Metallurgica. 35 (1987) 253–262. https://doi.org/10.1016/0001-6160(87)90233-1.
[84] D.N. Beshers, On the distribution of impurity atoms in the stress field of a dislocation, Acta Metallurgica. 6 (1958) 521–523. https://doi.org/10.1016/0001-6160(58)90166-4.
[85] J.P. Hirth, B. Carnahan, Hydrogen adsorption at dislocations and cracks in Fe, Acta Metallurgica. 26 (1978) 1795–1803. https://doi.org/10.1016/0001-6160(78)90092-5.
[86] A. Yaktiti, A. Dreano, R. Gass, T. Yvert, J.F. Carton, F. Christien, Modelling of hydrogen diffusion in a steel containing micro-porosity. Application to the permeation experiment, International Journal of Hydrogen Energy. 48 (2023) 14079–14094. https://doi.org/10.1016/j.ijhydene.2022.12.208.
[87] H. Nakagawa, T. Miyazaki, H. Yokota, Effects of aging temperature on the microstructure and mechanical properties of 1.8Cu-7.3Ni-15.9Cr-1.2Mo-low C, N martensitic precipitation hardening stainless steel, (n.d.) 9.

[88] W. Sha, A. Cerezo, G.D.W. Smith, Phase chemistry and precipitation reactions in maraging steels: Part IV. Discussion and conclusions, Metallurgical and Materials Transactions A. 24 (1993) 1251–1256. https://doi.org/10.1007/BF02668193.
[89] Z. Sun, Nano-sized precipitate stability and its controlling factors in a NiAl-strengthened ferritic alloy, Scientific Reports. (2015) 9.
[90] H. Brooks, Metal Interfaces, American Society for Metals. (1952) 20.
[91] S. Frappart, X. Feaugas, J. Creus, F. Thebault, L. Delattre, H. Marchebois, Study of the hydrogen diffusion and segregation into Fe–C–Mo martensitic HSLA steel using electrochemical permeation test, Journal of Physics and Chemistry of Solids. 71 (2010) 1467–1479. https://doi.org/10.1016/j.jpcs.2010.07.017.
[92] H.J. Grabke, E. Riecke, Absorption and diffusion of hydrogen in steels, MATERIALI IN TEHNOLOGIJE. (2000) 12.
[93] A.H.M. Krom, A. Bakker, Hydrogen trapping models in steel, Metall and Materi Trans B. 31 (2000) 1475–1482. https://doi.org/10.1007/s11663-000-0032-0.
[94] J. Völkl, G. Alefeld, Diffusion of hydrogen in metals, in: 1978: pp. 321–348.
[95] T. Schaffner, A. Hartmaier, V. Kokotin, M. Pohl, Analysis of hydrogen diffusion and trapping in ultra-high strength steel grades, Journal of Alloys and Compounds. 746 (2018) 557–566. https://doi.org/10.1016/j.jallcom.2018.02.264.
[96] J.-Y. Lee, S.M. Lee, Hydrogen trapping phenomena in metals with b.c.c. and f.c.c. crystal structures by the desorption thermal analysis technique, Surface and Coatings Technology. 28 (1986) 14.
[97] M. Nagano, Y. Hayashi, N. Ohtani, M. Isshiki, K. Igaki, HYDROGEN DIFFUSIVITY IN HIGH PURITY ALPHA IRON, Scripta METALLURGICA. 16 (1982) 4.
[98] B.D. Craig, On the elastic interaction of hydrogen with precipitates in lath martensite, Acta Metallurgica. 25 (1977) 1027–1030. https://doi.org/10.1016/0001-6160(77)90131-6.
[99] G. Hachet, J. Li, A.M. Hallil, A. Metsue, A. Oudriss, J. Bouhattate, X. Feaugas, A multi-scale analysis of the different interactions between defects and hydrogen: A review on the contribution of the elastic fields, Engineering Fracture Mechanics. 218 (2019) 106621. https://doi.org/10.1016/j.engfracmech.2019.106621.
[100] A.H. Cottrell, Constitutional vacancies in NiAl, Intermetallics. 3 (1995) 341–345. https://doi.org/10.1016/0966-9795(95)00015-Q.
[101] Yaojun A. Du, Lars Ismer, Jutta Rogal, Tilmann Hickel, Jörg Neugebauer, Ralf Drautz, First-principles study on the interaction of H interstitials with grain boundaries in α- and γ-Fe, Physical Review B. 84 (2011). https://doi.org/10.1103/PhysRevB.84.144121.
[102] A. Turk, S.D. Pu, D. Bombač, P.E.J. Rivera-Díaz-del-Castillo, E.I. Galindo-Nava, Quantification of hydrogen trapping in multiphase steels: Part II – Effect of austenite morphology, Acta Materialia. 197 (2020) 253–268. https://doi.org/10.1016/j.actamat.2020.07.039.
[103] M. Duportal, A. Oudriss, X. Feaugas, C. Savall, On the estimation of the diffusion coefficient and distribution of hydrogen in stainless steel, Scripta Materialia. 186 (2020) 282–286. https://doi.org/10.1016/j.scriptamat.2020.05.040.